# A Nonlinear Modal Aeroservoelastic Analysis Framework for Flexible Aircraft

Yinan Wang[*], Andrew Wynn[†] and Rafael Palacios[‡]

*Imperial College, London SW7 2AZ, United Kingdom*

**We present a nonlinear formulation in modal coordinates of the equations of motion of a flexible aircraft. It relies on the projection of the intrinsic equations of geometrically-nonlinear composite beams on the linear normal modes at a reference condition, which are coupled with 2D unsteady aerodynamics. The resulting description is suitable for nonlinear dynamic analysis and control design, while the description in modal coordinates links directly to linear aeroservoelastic analysis methods. Results are presented on and compared to cantilever wings and full aircraft configurations previously studied in the literature. Linear $\mathcal{H}_\infty$ control synthesis and closed-loop nonlinear simulations are finally explored on a highly-flexible flying wing under large-amplitude discrete gusts. Results show the ability of the proposed framework to capture the nonlinear dynamics of the aeroelastic system while providing a seamless integration with linear methods, and its strength in identification of the dominant contributors to the nonlinear response.**

## Nomenclature

$\mathbf{A}$: Linear modal coefficient matrix of aeroelastic system
$\mathcal{A}$: Linear operator in aerodynamic model
$A_j^{AE}$: Rational-function approximation coefficient to Theodorsen's function
$a$: Distance of aerodynamic centre to structural axis, normalised by $b$
$b$: Semi-chord of an aerofoil
$b_j^{AE}$: Rational-function approximation coefficient to Theodorsen's function
$\mathbf{C}$: Beam sectional compliance matrix
$C_D$: Aerofoil drag coefficient

[*]Postdoctoral Research Associate, Department of Aeronautics, AIAA Member
[†]Lecturer in Control, Department of Aeronautics
[‡]Reader in Aeronautics, Department of Aeronautics (contact author: rpalacio@imperial.ac.uk), AIAA Member

$C_k$: Theodorsen's function
$C_L$: Aerofoil lift coefficient
$C_M$: Aerofoil moment coefficient
$D_{AE}$: Aerodynamic drag
$\mathbf{e}$: The constant vector $\begin{bmatrix} 1 & 0 & 0 \end{bmatrix}^\top$
$\mathbf{f}$: Local sectional force vector
$\mathbf{f}_A$: Applied force and moment vector per unit length
$\mathbf{g}$: Gravity force
$\mathbf{H}$: Aerodynamic nonlinear coupling coefficients
$h$: Heaving displacement of aerofoil section
$\mathbf{K}$: $\mathcal{H}_\infty$ controller dynamics
$k_r$: Reduced frequency
$\mathbf{k}_0$: Initial curvature of the beam reference axis
$L_{AE}$: Aerodynamic lift
$\mathbf{M}$: Beam sectional mass matrix
$M_{AE}$: Aerodynamic moment
$\mathbf{m}$: Local sectional moment vector
$\mathbf{q}$: State vector of the aeroelastic system
$\mathbf{q}_{1g}$: Gust-induced velocity component in modal coordinates
$\mathbf{q}_a$: Aerodynamic states in modal coordinates
$\mathbf{q}_l$: Linearised states
$\mathbf{q}_1$: Velocity amplitude in modal coordinates
$\mathbf{q}_2$: Amplitude of sectional force resultants in modal coordinates
$\mathbf{r}$: Nodal displacement vector
$\mathbf{T}$: Coordinate transformation matrix from local to global frame
$\mathbf{u}_c$: Control input
$\mathbf{v}$: Local sectional velocity vector
$\hat{\mathbf{v}}$: Gust-induced relative velocity against local airflow
$V_\infty$: Freestream velocity
$\mathbf{w}_d$: External disturbance of linear state-space system
$\mathbf{x}_1$: Local velocity and angular velocity
$\mathbf{x}_2$: Local sectional force and moment resultants
$\mathbf{y}_c$: Performance output
$\mathbf{y}_m$: Measurements taken from the linear state-space system
$\mathbf{z}$: $\mathcal{H}_\infty$ controller states
$\alpha$: Angle of attack
$\boldsymbol{\Gamma}$: Structural nonlinear coupling coefficients
$\delta$: Control surface deflection
$\boldsymbol{\eta}_1$: External load in modal coordinates
$\boldsymbol{\Lambda}$: Linear modal coupling coefficient matrix
$\lambda_j$: Unsteady aerodynamic state
$\rho$: Air density
$\boldsymbol{\phi}_1$: Modal basis in $\mathbf{x}_1$
$\boldsymbol{\phi}_2$: Modal basis in $\mathbf{x}_2$
$\boldsymbol{\Psi}$: Infinitesimal rotation vector
$\boldsymbol{\omega}$: Local sectional angular velocity vector
$\omega$: Aerofoil angular velocity
$\bullet'$: Derivative w.r.t. $s$ (beam arclength)
$\dot{\bullet}$: Derivative w.r.t. $t$ (time)
$\tilde{\bullet}$: Cross-product operator

# I. Introduction

High-altitude, long-endurance aircraft often feature flexible, high-aspect ratio wings to improve their aerodynamic efficiency and endurance. Large dynamic deformations during flight as a result of their structural flexibility, and the resulting coupling between structural and flight dynamics, are therefore key challenges particular to this class of aircraft.[1] To understand and safely accommodate these effects during design, one needs numerical models that incorporate geometrically-nonlinear structural effects.

For this purpose, a number of simulation frameworks for very flexible aircraft have been created that typically employ geometrically-nonlinear beam models to represent the structural response, coupled with low-order aerodynamic descriptions, in order to reduce the coupled nonlinear aeroelastic problem to a manageable size for time-domain computations. Early works included that by Drela[2] using a displacement-based beam model with lifting-line theory. More recent works have seen the aerodynamic model simplified to strip theory[3,4] or extended to full inviscid 3D flow using unsteady vortex-lattice methods.[5,6] The structural models have also seen the use of other variants of geometrically-exact beam theories including mixed-formulation,[7] strain-based[8] and intrinsic beam theories.[6] An overview of the key methodologies in structural and aerodynamic models was carried out by Palacios *et al.*[9]

Despite these developments, full-vehicle simulations require models which possess thousands of degrees-of-freedom and complex nonlinear couplings between them. Thus, there is a strong incentive to reduce the dimension complexity of the nonlinear model in order to gain insight into the design, analysis and control of these aircraft. Nonlinear model reduction methods on structural dynamics systems have been recently reviewed by Mignolet *et al.*,[10] with a particular focus on problems described by existing FE analysis tools. There are several alternatives in which a nonlinear reduced-order system can be obtained from a FE model, which include direct computation of the nonlinear coupling between modes in the reduced basis via the appropriate nonlinear element formulation, or, if this is not possible, by a regression analysis with either a prescribed displacement field or force distributions on the structure. Past works indicated that the selection of the basis for reduction is critical,[10,11] and studies typically use linear normal modes and related bases including Ritz vectors, as well as POD-based basis (which must be obtained from prior nonlinear simulations of the system). The efficacy of each choice of modal basis is dependent on the problem and loading of the structure.

In comparison, nonlinear model reduction of aerodynamic models is considerably more difficult. Placzek *et al.*[12] demonstrated such reductions using POD, but also noted robustness issues in identifying a nonlinear reduced-order model. Reviews by Lucia *et al.*[13] and Dowell *et al.*[14] both addressed nonlinear model reduction methods on nonlinear aeroelastic systems. One approach that is relevant to flexible aircraft is to couple nonlinear reduced-order aerodynamic models to a cross-section geometry with only rigid-body degrees of freedom,[15] or, extending the approach to a slender wing with a fixed cross-section geometry.[16] Another such approach is to couple a linear reduced-order aerodynamic model to a nonlinear reduced-order 3D structural model,[17] in addition to the use of beam-type structural descriptions reviewed above.

In this paper we propose a nonlinear aeroelastic simulation framework that uses linear normal modes as primary variables to describe the geometrically-nonlinear structural response, linking nonlinear aeroelastic modelling with existing modal information used in linear aeroelastic analysis. This choice enables the simulation and analysis of the full-order aeroelastic system, while implicitly using a modal basis that is suitable for direct nonlinear model reduction. The method uses a nonlinear structural model based on the intrinsic formulation for beams that is projected onto the structural modal basis, with the intrinsic formulation of beams was first described by Hodges[18] and the modal projection described by Wynn *et al.*[19]. In a separate work[20] we have described the use of a linear 3D FE model to create such an intrinsic beam description of the structure, which is then coupled with a 2D unsteady aerodynamic model. The aerodynamic model is also projected onto the structural model using the inflow model that relates the local aerodynamic forces to the local velocity of the aerofoil in still air.[21] This paper subsequently validates numerical results from the proposed framework against established test cases. Following this, a control design process and flight dynamic simulations will be used to demonstrate the capabilities of this description when applied to an actual design scenario. We further demonstrate the extraction of modal and nonlinear coupling information from the time-domain simulation, which will identify the source of the contributions to the observed nonlinear dynamics and also justify the choice of projecting the aerodynamic couplings onto the structural natural modes.

# II. Aeroelastic System

## II.A. Intrinsic Structural Model

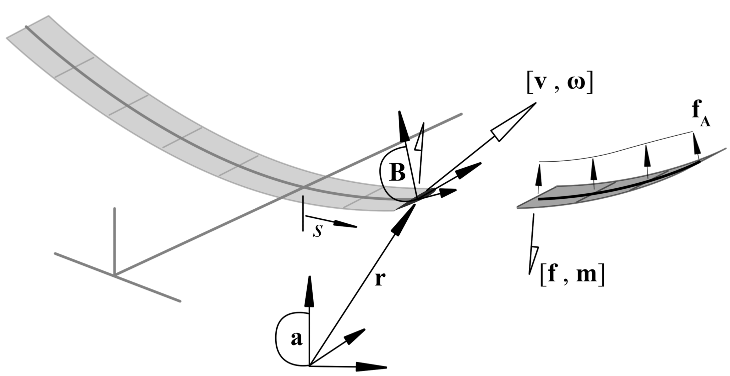


**Figure 1. Degrees of freedom and frames of reference of the intrinsic beam formulation applied to an aircraft-like structure.**

The intrinsic beam equations describe evolution of the sectional inertial **v** and angular velocities $\boldsymbol{\omega}$, and sectional internal forces $\mathbf{f}$ and moments $\mathbf{m}$ (that is, the sectional stress resultants) at each location $s$ along a beam assembly. All are three-element vectors expressed in the local deformed frame of reference ($B$-frame in Figure 1). By writing $\mathbf{x}_1 = [\ \mathbf{v}^\top \quad \boldsymbol{\omega}^\top\ ]^\top$ and $\mathbf{x}_2 = [\ \mathbf{f}^\top \quad \mathbf{m}^\top\ ]^\top$, the intrinsic equations assume the form of[20]

$$\begin{aligned} \mathbf{M}\dot{\mathbf{x}}_1 - \mathbf{x}_2' - \mathbf{E}\mathbf{x}_2 + \mathcal{L}_1(\mathbf{x}_1)\mathbf{M}\mathbf{x}_1 + \mathcal{L}_2(\mathbf{x}_2)\mathbf{C}\mathbf{x}_2 &= \mathbf{f}_A, \\ \mathbf{C}\dot{\mathbf{x}}_2 - \mathbf{x}_1' + \mathbf{E}^\top\mathbf{x}_1 - \mathcal{L}_1^\top(\mathbf{x}_1)\mathbf{C}\mathbf{x}_2 &= \mathbf{0}. \end{aligned} \tag{1}$$

In the above equation, $\mathbf{x}'$ indicates a spatial derivative of $\mathbf{x}$, while $\dot{\mathbf{x}}$ indicates its time derivative. The functions $\mathcal{L}_i$ are linear operators defined in Wynn *et al.*[19] and the matrix $\mathbf{E} = \mathcal{L}_1([\ \mathbf{e}^\top \quad \mathbf{k}_0^\top\ ]^\top)$, where $\mathbf{e} = [\ 1 \quad 0 \quad 0\ ]^\top$ is a constant vector containing information on the direction of the reference line relative to the local frame of reference (defined to always be the local x-axis). The initial curvature of the beam reference axis is $\mathbf{k}_0(s)$. The material property matrices $\mathbf{M}$ and $\mathbf{C}$, which in general will vary along the beam axis, describe the beam section's inertia and compliance at each location $s$. Definitions of these quantities can be found in Palacios *et al.*[20] . A modal projection of the equation is used in this work so that modal amplitudes become the primary variables, making extraction of modal information from time-domain simulations trivial. Additionally nonlinear model reduction can be carried out with less effort (by using a subset of the full description that is cast in natural modes), and that linearisation can also be made easily for the purpose of linear state-space system creation and control synthesis. We define the modal projection of the states as[19]

$$\begin{aligned} \mathbf{x}_1 &= \sum_j \boldsymbol{\phi}_{1j} q_{1j}, \\ \mathbf{x}_2 &= \sum_j \boldsymbol{\phi}_{2j} q_{2j}, \end{aligned} \tag{2}$$

which recasts the problem using the states $q_{1j}$ and $q_{2j}$, that is, the modal amplitudes in velocities/angular velocities and stress/moment resultants, respectively, with $\boldsymbol{\phi}_{1i}$ and $\boldsymbol{\phi}_{2i}$ being the corresponding natural modes (eigenfunctions of the linear operator associated with linearising (1)) in velocity and force variables. Note that $\boldsymbol{\phi}_{1i}$ and $\boldsymbol{\phi}_{2i}$ are effectively the components of the same set of natural modes. We also assume that $\boldsymbol{\phi}_{1i}$ and $\boldsymbol{\phi}_{2i}$ are normalised with the mass and stiffness matrices, respectively.[19] This formulation does not make an explicit distinction between structural and rigid-body velocity modes, and both are elements of $\boldsymbol{\phi}_{1i}$. By defining the vector of modal amplitudes $\mathbf{q} = \left(\begin{smallmatrix}\mathbf{q}_1 \\ \mathbf{q}_2\end{smallmatrix}\right)$, the nonlinear finite-dimensional equations of motion can be written as[19]

$$\dot{\mathbf{q}} = \mathbf{A}^{-1}\left((\boldsymbol{\Lambda} + \boldsymbol{\Gamma}(\mathbf{q}))\,\mathbf{q} + \left(\begin{smallmatrix}\boldsymbol{\eta}_1 \\ 0\end{smallmatrix}\right)\right), \tag{3}$$

with constant matrices $\mathbf{A}$, $\mathbf{\Lambda}$ and a linear operator $\mathbf{\Gamma}$ whose coefficients are spatial integrals of the modes ($\boldsymbol{\phi}_1$, $\boldsymbol{\phi}_2$) and the material properties of the beam structure ($\mathbf{M}$ and $\mathbf{C}$). The $\boldsymbol{\eta}_1$ term refers to the modal projection of the applied forces.

Finally, the displacement (displacement vector $\mathbf{r}$) and rotation (cartesian rotation matrix $\mathbf{T}$ from the inertial $a$-frame to the element local $B$-frame) variables at each point on the structure, shown in Figure 1, can be reclaimed through an integration of either velocity with respect to time,

$$
\begin{aligned}
\dot{\mathbf{T}} &= \mathbf{T}\tilde{\boldsymbol{\omega}} = \mathbf{T}\sum_{j=1}^{\infty} \tilde{\boldsymbol{\phi}}_{1j}|_{456} q_{1j}, \\
\dot{\mathbf{r}} &= \mathbf{T}\mathbf{v} = \mathbf{T}\sum_{j=1}^{\infty} \boldsymbol{\phi}_{1j}|_{123} q_{1j},
\end{aligned}
\tag{4}
$$

or strain with respect to space,

$$
\begin{aligned}
\mathbf{T}' &= \mathbf{T}\left(\sum_{j=1}^{\infty} \widetilde{\mathbf{C}\boldsymbol{\phi}_{2j}}|_{456} q_{2j} + \tilde{\mathbf{k}}_0\right), \\
\mathbf{r}' &= \mathbf{T}\left(\sum_{j=1}^{\infty} (\mathbf{C}\boldsymbol{\phi}_{2j})|_{123} q_{2j} + \mathbf{e}\right),
\end{aligned}
\tag{5}
$$

where in these equations the number subscripts indicate the components taken from the respective variable. The tilde is the cross-product operator that transforms a 3-dimensional vector into a $3 \times 3$ matrix such that $\tilde{\mathbf{a}}\mathbf{b} = \mathbf{a} \times \mathbf{b}$.

### II.B. 2D Unsteady Aerodynamic Formulation

Linear unsteady aerofoil theory is used to derive the coupled aeroelastic model. It relates the aerodynamic forces on a 2D aerofoil section, subject to a freestream airflow of a constant velocity (airspeed), to the effective angle of attack of the aerofoil. The unsteady aerodynamic forces will be obtained via an inviscid analysis on a flat 2D aerofoil using the small disturbance approximation (Theodorsen's solution), with the solution then modified to fit actual parameters of the aerofoil shape.

For an aerofoil with chord $2b$ moving through air with a velocity $V_\infty$, the aerodynamic

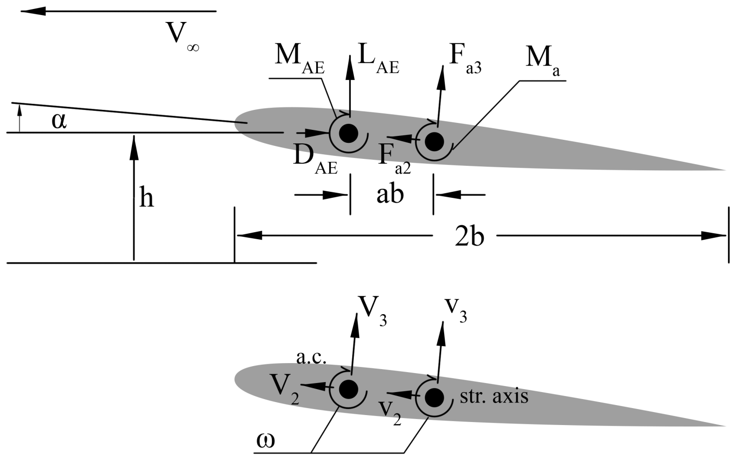


**Figure 2. Definitions of the 2D aerofoil problem. For clarity, the top figure indicates the relevant aerodynamic force components whereas and bottom figure indicates relevant velocity components.**

lift, drag and moment under linear assumptions will be expressed as

$$L_{AE} = \frac{1}{2}\rho V_\infty^2 \cdot 2b \cdot (C_{L0} + \Delta C_L), \tag{6a}$$

$$D_{AE} = \frac{1}{2}\rho V_\infty^2 \cdot 2b \cdot C_{D0}, \tag{6b}$$

$$M_{AE} = \frac{1}{2}\rho V_\infty^2 \cdot 2b \cdot 2b \cdot (C_{M0} + \Delta C_M), \tag{6c}$$

where $\Delta\overline{C}_L = \overline{C}_{L\alpha}\overline{\alpha}_{eq} + C_{L\delta}\overline{\delta}$ and $\Delta\overline{C}_M = \overline{C}_{M\alpha}\overline{\alpha}_{eq} + C_{M\delta}\overline{\delta}$ and an overline indicates a frequency-domain variable. Here, $\overline{\alpha}_{eq} = \overline{\alpha} - \dot{\overline{h}}/V_\infty + \dot{\overline{\alpha}}b/V_\infty$ is the effective angle of attack and we model control surface actions as an instantaneous, linear change in the aerodynamic coefficients with respect to a control surface deflection angle $\delta$. The aerodynamic coefficients follow their usual definitions. For simplicity, in the current model we assume that there are no unsteady effects associated with control surface deflection, i.e. $C_{L\delta}$ and $C_{M\delta}$ are constants. Unsteady effects associated with control surfaces are straightforward to incorporate if necessary. We describe the unsteady terms $\overline{C}_{L\alpha}\overline{\alpha}_{eq}$ and $\overline{C}_{M\alpha}\overline{\alpha}_{eq}$ using Theodorsen's solution. The motion of the aerofoil against still air can also be described in terms of its rigid-body velocity in the aerofoil's local reference frame, with the axes local to the aerofoil and origin on the aerodynamic centre. Thus we also define the transverse velocity $V_2$ (positive forward) parallel to the chordline, normal velocity $V_3$ (positive up), and angular velocity $\omega$ (positive pitch-up).

The flat aerofoil undergoing heaving and pitching motions experiences aerodynamic forces that are expressed, in frequency-domain, as[22]

$$\overline{L}_{AE}(ik_r) = \pi\rho V_\infty 2bC_k(ik_r)[V_\infty\overline{\alpha}(ik_r) - \overline{\dot{h}}(ik_r) + b\overline{\dot{\alpha}}(ik_r)], \tag{7a}$$

$$\overline{M}_{AE}(ik_r) = -\frac{1}{2}\pi\rho b^2[V_\infty b\overline{\dot{\alpha}}(ik_r)]. \tag{7b}$$

The reduced (non-dimensional) time is defined as $s_r = \frac{tV_\infty}{b}$ and the corresponding reduced frequency $k_r = \omega^* V_\infty/b$ with $\omega^*$ being angular frequency. The lift deficiency function $C_k$ will be approximated in the usual manner,

$$C_k(ik_r) = 1 - \sum_{j=1}^{N_{AE}} \frac{ik_r A_j^{AE}}{ik_r + b_j^{AE}} \tag{8}$$

where for a given $N_{AE}$, the sum of coefficients $A_j^{AE}$ always equals 1/2. It is important to note that this solution has not included the effects of apparent mass, which would give additional terms multiplying $\overline{\ddot{h}}$, $\overline{\dot{\alpha}}$ and $\overline{\ddot{\alpha}}$. Apparent mass if often neglected and this is done here too to simplify our description, although there is no fundamental reason why it could not be included. Using small-angle approximation and assuming $V_\infty$ varies slowly with time, that is $V_\infty = V_2/\cos\alpha \approx V_2$, we obtain

$$\dot{h} = V_3\cos\alpha + V_2\sin\alpha \approx V_3 + V_2\alpha, \tag{9a}$$

$$\dot{\alpha} = \omega. \tag{9b}$$

Combining (7), (8) and (9), and transforming to time domain, we have

$$L_{AE} = 2\pi\rho V_\infty b\left[\frac{1}{2}(-V_3 + b\omega) + V_\infty \sum A_j^{AE} b_j^{AE}\lambda_j\right], \tag{10a}$$

$$M_{AE} = -2\pi\rho V_\infty b^2 \cdot \frac{b}{4}\omega, \tag{10b}$$

where we have introduced a set of aerodynamic states $\lambda_j$ corresponding to each coefficient in the rational approximation to Theodorsen's function. They are obtained from solving

$$\dot{\lambda}_j + \frac{b_j^{AE}V_\infty}{b}\lambda_j = -\frac{1}{b}V_3 + \omega. \tag{11}$$

Eqs. (10) and (11) provide a complete description of the aerodynamic loads in terms of aerofoil velocities defined in the local aerodynamic reference frame. Similar solutions can also be found in the literature[23] although small differences may arise depending on details of small-angle approximations.

Next, we will express the aerodynamic loads in terms of the local velocities computed in the intrinsic beam model. We start by substituting the solution of the unsteady aerodynamic forces (10) obtained previously into (6), to obtain

$$L_{AE} = \frac{1}{2}\rho V_\infty \cdot 2b\left(C_{L\alpha}(\frac{1}{2}(-V_3 + b\omega) + \frac{1}{2}V_\infty \sum_{j=1}^{N_{AE}} 2A_j^{AE} b_j^{AE} \lambda_j) + V_\infty(C_{L0} + C_{L\delta}\delta)\right), \quad (12a)$$

$$D_{AE} = \frac{1}{2}\rho V_\infty^2 \cdot 2bC_{D0}, \quad (12b)$$

$$M_{AE} = -\frac{1}{2}\rho V_\infty \cdot 2b \cdot 2bC_{L\alpha}\frac{b}{8}\omega + \frac{1}{2}\rho V_\infty^2 \cdot 2b \cdot 2b(C_{M0} + C_{M\delta}\delta). \quad (12c)$$

We now express the velocities about the aerodynamic centre ($V_2$, $V_3$, $\omega$) as velocities about the structural axis ($v_2$, $v_3$, $\omega$). For this we define the structural axis being a point on the chord *aft* of the aerodynamic centre located with a distance of $ab$ from the a.c. where $a$ is the ratio of this distance to the length of half-chord (a negative $a$ indicates the structural axis is forward of the a.c.). At the structural axis, we define the transverse velocity $v_2$ (positive forward) parallel to the chordline, normal velocity $v_3$ (positive up) perpendicular to the chordline and angular velocity $\omega$ around the aerodynamic centre (positive pitch-up), together with associated loads measured at the structural axis being $F_{a2}$ normal to the chord, $F_{a3}$ parallel to the chord and the moment $M_a$. The transformation is written as

$$V_2 = V_\infty = v_2, \quad (13a)$$

$$V_3 = v_3 + ab\omega. \quad (13b)$$

The aerodynamic lift $L_{AE}$, drag $D_{AE}$ forces and moment $M_{AE}$ are also transformed into the local frame of the aerofoil around the structural axis, $F_{a2}$, $F_{a3}$ and $M_a$. In this process the angle of attack is expressed as ratios between the freestream velocity and its individual components, resulting in

$$F_{a2} = -\frac{1}{V_\infty}(v_3 L_{AE} + v_2 D_{AE}), \quad (14a)$$

$$F_{a3} = \frac{1}{V_\infty}(v_2 L_{AE} - v_3 D_{AE}), \quad (14b)$$

$$M_a = M_{AE} + abL_{AE}. \quad (14c)$$

We shall then define the force state and the instantaneous sectional velocity state in the local structural reference frame, respectively, as

$$\begin{aligned} \mathbf{f}_a &= \begin{bmatrix} 0 & F_{a2} & F_{a3} & M_a & 0 & 0 \end{bmatrix}^\top, \\ \mathbf{x}_1 &= \begin{bmatrix} v_1 & v_2 & v_3 & \omega_1 & \omega_2 & \omega_3 \end{bmatrix}^\top, \end{aligned} \quad (15)$$

with $\omega = \omega_1$, both consistent to the definition of external force and velocity state in the intrinsic beam formulation in equation (1) ($v_1$, $\omega_2$ and $\omega_3$ have no effect on the aerodynamic forces in this sectional aerodynamic model). This finally allows to relate the local rigid-body velocities at the structural axis to the local aerodynamic loads generated by these velocities and leads to a compact matrix form of the aerodynamics, both consistent to the definition of external force and velocity state in the intrinsic beam formulation in equation (1) ($v_1$, $\omega_2$ and $\omega_3$ have no effect on the aerodynamic forces under 2-D assumptions). This results in

$$\mathbf{f}_a = \rho b(\mathcal{A}_1(\mathbf{x}_1)\mathbf{x}_1 + V_\infty \mathcal{A}_2 \mathbf{x}_1 \cdot \sum_{j=1}^{N_{AE}} 2A_j^{AE} b_j^{AE} \lambda_j + \mathcal{A}_3(\mathbf{x}_1)\mathbf{x}_1 \cdot \delta), \tag{16a}$$

$$\dot{\lambda}_j = \boldsymbol{\kappa}_{AE}^\top \mathbf{x}_1 - \frac{b_j^{AE} V_\infty}{b} \lambda_j, \tag{16b}$$

with vector $\boldsymbol{\kappa}_{AE}^\top = \begin{bmatrix} 0 & 0 & -1/b & (1-a) & 0 & 0 \end{bmatrix}$ and the linear aerodynamic operators being

$$\mathcal{A}_1(\mathbf{x}_1) = \tag{17a}$$
$$\begin{pmatrix} 0 & 0 & 0 & 0 & 0 & 0 \\ 0 & -C_{D0}v_2 & \frac{C_{L\alpha}}{2}v_3 - C_{L0}v_2 & -b(1-a)\frac{C_{L\alpha}}{2}v_3 & 0 & 0 \\ 0 & C_{L0}v_2 - (\frac{C_{L\alpha}}{2} + C_{D0})v_3 & 0 & b(1-a)\frac{C_{L\alpha}}{2}v_2 & 0 & 0 \\ 0 & b((2C_{M0} + aC_{L0})v_2 - a\frac{C_{L\alpha}}{2}v_3) & 0 & b^2(a - a^2 - \frac{1}{2})\frac{C_{L\alpha}}{2}v_2 & 0 & 0 \\ 0 & 0 & 0 & 0 & 0 & 0 \\ 0 & 0 & 0 & 0 & 0 & 0 \end{pmatrix},$$

$$\mathcal{A}_2 = \begin{pmatrix} 0 & 0 & 0 & 0 & 0 & 0 \\ 0 & 0 & -1 & 0 & 0 & 0 \\ 0 & 1 & 0 & 0 & 0 & 0 \\ 0 & ab & 0 & 0 & 0 & 0 \\ 0 & 0 & 0 & 0 & 0 & 0 \\ 0 & 0 & 0 & 0 & 0 & 0 \end{pmatrix}, \tag{18}$$

$$
\mathcal{A}_3(\mathbf{x}_1) = \begin{pmatrix} 0 & 0 & 0 & 0 & 0 & 0 \\ 0 & 0 & -C_{L\delta}v_2 & 0 & 0 & 0 \\ 0 & C_{L\delta}v_2 & 0 & 0 & 0 & 0 \\ 0 & (abC_{L\delta}+2bC_{M\delta})v_2 & 0 & 0 & 0 & 0 \\ 0 & 0 & 0 & 0 & 0 & 0 \\ 0 & 0 & 0 & 0 & 0 & 0 \end{pmatrix}. \tag{19}
$$

Note finally that the reference velocity, $V_\infty$, has been retained in (16), instead of being replaced by the local velocity, $v_2$, as we regard changes in the aerodynamic lag due to changes in freestream velocity negligible in the problems of interest. As a result, we have arrived at a description based on Theodorsen's solution (without apparent mass) that provides a relation between the aerodynamic loads on a 2D aerofoil section and its velocities relative to still air, all expressed in a local reference frame. We should however note that other linear unsteady aerodynamic formulations written in terms of local downwash could have been also been equally employed.

### II.C. Modal Projection of the Unsteady Aerodynamic Loadings

We are now ready to project the aerodynamic forces onto the structural modes as added couplings in the nonlinear modal formulation. The starting point is the unsteady aerodynamic forces expressed in the local frame (16), which can be regarded as an expression of local aerodynamic loads $\mathbf{f}_a(\mathbf{x}_1)$ in terms of local velocities $\mathbf{x}_1$. The projection process has a number of requirements. The first requirement is that the chord of the lifting surface(s) must be constant in order for the unsteady terms to be projected onto global modes due to the nature of the unsteady aerodynamic model used here. Another requirement is that the undeformed structural axis system ($\mathbf{B}$ in Figure 1 under zero external load), formed with local axes $\mathbf{b}_1$, $\mathbf{b}_2$ and $\mathbf{b}_3$, should have the local $\mathbf{b}_2$ and $\mathbf{b}_3$ axes lie in the same plane as the aerofoil cross-section with $\mathbf{b}_2$ pointing in the zero-lift direction. Note that it is easy to modify the beam axis definition so that the last requirement is satisfied.

We begin by substituting (2) into (16) and obtain

$$
\begin{aligned}
\mathbf{f}_a = \rho b \Bigg( & \mathcal{A}_1\Big(\sum_{k=1}^{\infty} \boldsymbol{\phi}_{1k} q_{1k}\Big) \sum_{l=1}^{\infty} \boldsymbol{\phi}_{1l} q_{1l} + V_\infty \mathcal{A}_2 \sum_{k=1}^{\infty} \boldsymbol{\phi}_{1k} q_{1k} \cdot \sum_{l=1}^{N_{AE}} 2A_l^{AE} b_l^{AE} \lambda_l \\
& + \mathcal{A}_3\Big(\sum_{k=1}^{\infty} \boldsymbol{\phi}_{1k} q_{1k}\Big) \sum_{l=1}^{\infty} \boldsymbol{\phi}_{1l} q_{1l} \cdot \delta \Bigg), && \text{(20a)} \\
\dot{\lambda}_j = \boldsymbol{\kappa}_{AE}^\top & \sum_{k=1}^{\infty} \boldsymbol{\phi}_{1k} q_{1k} - \frac{b_j^{AE} V_\infty}{b} \lambda_j. && \text{(20b)}
\end{aligned}
$$

For the second equation above, we further split $\lambda_j$ into components corresponding to each velocity mode $\boldsymbol{\phi}_{1k}$ as

$$\lambda_j = \sum_{k=1}^{\infty} \boldsymbol{\kappa}_{AE}^{\top} \boldsymbol{\phi}_{1k} q_{a,jk}, \tag{21}$$

converting the time evolution equation into

$$\dot{q}_{a,jk} = q_{1k} - \frac{b_j^{AE} V_\infty}{b} q_{jk}. \tag{22}$$

We then insert the aerodynamic forcing into the external forcing term and define the modal aerodynamic forcing as

$$\eta_{1a,j} = \int_S \boldsymbol{\phi}_{1j}^{\top} \mathbf{f}_a \, ds. \tag{23}$$

Using Einstein's summation convention, this can be written as

$$\eta_{1a,j} = \mathrm{H}_{1,jkl} q_{1k} q_{1l} + V_\infty \mathrm{H}_{2,jklm} q_{1k} q_{a,lm} + \mathrm{H}_{3,jkl,d} q_{1k} q_{1l} \cdot \delta_d, \tag{24}$$

where

$$\mathrm{H}_{1,jkl} = \int_S \rho b \boldsymbol{\phi}_{1j}^{\top} \mathcal{A}_1(\boldsymbol{\phi}_{1k}) \boldsymbol{\phi}_{1l} \, ds, \tag{25a}$$

$$\mathrm{H}_{2,jklm} = \int_S \rho b \boldsymbol{\phi}_{1j}^{\top} \mathcal{A}_2 \boldsymbol{\phi}_{1k} \cdot 2 A_l^{AE} b_l^{AE} \boldsymbol{\kappa}_{AE}^{\top} \boldsymbol{\phi}_{1m} \, ds, \tag{25b}$$

$$\mathrm{H}_{3,jkl,d} = \int_S \rho b \boldsymbol{\phi}_{1j}^{\top} \mathcal{A}_{3,d}(\boldsymbol{\phi}_{1k}) \boldsymbol{\phi}_{1l} \, ds, \tag{25c}$$

with $j, k, m = 1, \ldots, N_M$, $l = 1, \ldots, N_{AE}$ and $d = 1, \ldots, N_d$ and $N_M$, $N_{AE}$ and $N_d$ being number of structural modes, aerodynamic lag terms and number of independent control surfaces respectively.

Note here an additional index $d$ is added to the $\mathcal{A}_3$ operators. This is to account for the existence of multiple control surfaces, each of them creating their own set of $\mathcal{A}_3$ operators. Similarly the other aerodynamic coefficients including $C_{L\alpha}$, $C_{M0}$ and $C_{L\delta}$ are now all dependent on the location along the beam ($s$) which means the $\mathcal{A}$ operators are also $s$-dependent. We finally insert Equation (23) into the structural equations (3) which results in the modal aeroelastic system, truncated to a finite number of modes, as

$$\dot{\mathbf{q}}_1 = \mathbf{A}_1^{-1} \left( \boldsymbol{\Lambda}_1 \mathbf{q}_2 - (\boldsymbol{\Gamma}_1(\mathbf{q}_1) - \mathbf{H}_1(\mathbf{q}_1) - V_\infty \mathbf{H}_2(\mathbf{q}_a) - \mathbf{H}_{3,d}(\mathbf{q}_1)\delta_d) \mathbf{q}_1 - \boldsymbol{\Gamma}_2(\mathbf{q}_2) \mathbf{q}_2 \right), \tag{26a}$$

$$\dot{\mathbf{q}}_2 = \mathbf{A}_2^{-1} (\boldsymbol{\Lambda}_2 \mathbf{q}_1 + \boldsymbol{\Gamma}_3(\mathbf{q}_1) \mathbf{q}_2), \tag{26b}$$

$$\dot{\mathbf{q}}_a = \mathbf{D}(\mathbf{J}) \mathbf{q}_1 - V_\infty \mathbf{D}(\mathbf{P}) \mathbf{q}_a, \tag{26c}$$

where we have defined the vector $\mathbf{q}_a$ by concatenation of all aerodynamic states $q_{a,jk}$. Similar to the structural coupling operators $\mathbf{\Gamma}$, the aerodynamic load operators are defined as

$$\mathbf{H}_1(\mathbf{q}_1)|_{jl} = \sum_{k=1}^{N_M} \mathrm{H}_{1,jkl} q_{1k}, \tag{27a}$$

$$\mathbf{H}_2(\mathbf{q}_a)|_{jk} = \sum_{l=1}^{N_{AE}} \sum_{m=1}^{N_M} \mathrm{H}_{2,jklm} q_{a,lm}, \tag{27b}$$

$$\mathbf{H}_{3,d}(\mathbf{q}_1)|_{jl} = \sum_{k=1}^{N_M} \mathrm{H}_{3,jkl,d} q_{1k}. \tag{27c}$$

Finally, $\mathbf{D}(\mathbf{J})$ and $\mathbf{D}(\mathbf{P})$ are block diagonal matrices containing $N_{AE}$ blocks of matrices $\mathbf{J}$ and $\mathbf{P}$, respectively. The single-column matrix $\mathbf{J}$ is the same size as velocity state vector $\mathbf{q}_1$ with every element being unity and the diagonal matrix $\mathbf{P}|_{jj} = b_j^{AE}/b$. The freestream velocity $V_\infty$ is a global scalar value defined as the local velocity at a node chosen as reference. Equation (26) is thus a closed-form modal aeroelastic formulation for flexible aircraft. Its application will be demonstrated by the numerical results presented in Section IV.

### II.D. Flight Dynamics Description

In order to create a description that can be used to model the full-vehicle flight-dynamics response, the effect of gravity, atmospheric gust, and engine thrust must be also accounted for. Weight is a constant vector in the global reference frame. Its effect on the intrinsic variables is computed by transforming the constant vector into the local reference frame using the transformation matrix defined in (4). If $\mathbf{g}_0$ is the constant gravity vector in the global frame, when projected onto the modes, it influences the $j$-th velocity mode $q_{1j}$ as a contribution to the external force term,

$$\eta_{g,j} = \int_S \boldsymbol{\phi}_{1j}^\top \mathbf{T}^\top \mathbf{M} \begin{pmatrix} \mathbf{g}_0 \\ \mathbf{0} \end{pmatrix} ds. \tag{28}$$

This is a linear function of the rotation matrix, $\mathbf{T}$, thus we can also write the influence of gravity in vector form as $\boldsymbol{\eta}_g = \mathbf{H}_g(\mathbf{T})$ which will appear in the forcing term $\boldsymbol{\eta}$ in the equation of motion.

The thrust vector is modelled as a follower force (since propulsion devices move with the local airframe) exerted at the locations $s_n$ on which the engine/pods are assumed to be mounted. It is another constant external force contribution, but defined in the local frame as

$$\eta_{T,j} = \sum_{n=1}^{N_T} \boldsymbol{\phi}_{1j}^{\top}\Big|_{s=s_n} \mathbf{f}_{t,n}. \tag{29}$$

The vector $\mathbf{f}_{t,n} = \mathbf{f}_{t0,n} f_n$ describes a 6-element thrust force/moment vector of magnitude $f_n$ and direction $\mathbf{f}_{t0,n}$ with a total of $N_T$ thrust vectors. In order for changes in thrust to be considered, the influence can be written as a vector $\boldsymbol{\eta}_T = \mathbf{H}_T \mathbf{f}_T$ where $\mathbf{f}_T$ is the collection of $f_n$ which will also appear in the forcing term in the equation of motion.

In section II.B, the aerodynamic loads have been computed by assuming that the aerofoil section is moving through still air. We will include the effect of an external gust, $\mathbf{v}_g(\mathbf{r}, t)$, defined as a spatial gust distribution of gust velocities in the global frame, as causing an additional downwash as a local gust velocity. The relative local velocity will be $\mathbf{v} - \mathbf{T}^{\top}\mathbf{v}_g$, and in this work we split the gust profile into a linear combination of fixed spatial distributions $\mathbf{v}_{g,i}(\mathbf{r})$ and their intensities $w_{g,i}(t)$, which gives

$$\mathbf{v}_g(\mathbf{r}, t) = \sum_i \mathbf{v}_{g,i}(\mathbf{r}) w_{g,i}(t). \tag{30}$$

It should be noted that this form retains the generality of the gust model if a space-spanning basis is used for $\mathbf{v}_{g,i}$, although this work we use the particular gust profiles that are of interest in the simulation. The corresponding modal amplitude is rewritten as:

$$q_{1j}^{*} = q_{1j} - \sum_i \int_S \boldsymbol{\phi}_{1j}^{\top}|_{123} \mathbf{T}^{\top} \mathbf{v}_{g,i}(\mathbf{r}) w_{g,i} \, ds, \tag{31a}$$

where $\mathbf{r}(s)$ is the spatial location of a given point on the beam's reference axis. The above relation can be written in vector form as

$$\mathbf{q}_1^{*} = \mathbf{q}_1 + \mathbf{q}_{1g} = \mathbf{q}_1 + \mathbf{Q}_{1g} \mathbf{w}_g, \tag{32}$$

where $\mathbf{Q}_{1g}$ is a matrix which depends upon the chosen (fixed) spatial gust distribution $\mathbf{v}_{g,i}$. It is worth noting that this new modal amplitude in velocities affects only the computation of the aerodynamic forces.

Finally, the time integration of displacement and rotation (4) are linear in both rotation $\mathbf{T}$ and velocity state $\mathbf{q}_1$ and therefore there exist linear operators $\mathbf{N}_R$ and $\mathbf{N}_D$ so that

$$\dot{\mathbf{T}}_v = \mathbf{N}_R(\mathbf{T}) \mathbf{q}_1, \tag{33a}$$

$$\dot{\mathbf{r}} = \mathbf{N}_D(\mathbf{T}) \mathbf{q}_1. \tag{33b}$$

Here $\mathbf{T}_v$ denotes $\mathbf{T}$ rearranged into a vector form. By combining equations (26), (28), (29),

(32) and (33), the final assembled equation of the aeroelastic system is written as:

$$\begin{aligned}
\dot{\mathbf{q}}_1 = \mathbf{A}_1^{-1} [&\mathbf{\Lambda}_1\mathbf{q}_2 - \mathbf{\Gamma}_1(\mathbf{q}_1)\mathbf{q}_1 - \mathbf{\Gamma}_2(\mathbf{q}_2)\mathbf{q}_2 + \\
&(\mathbf{H}_1(\mathbf{q}_1^*) + V_\infty\mathbf{H}_2(\mathbf{q}_a) + \mathbf{H}_{3,d}(\mathbf{q}_1^*)\delta_d)\,\mathbf{q}_1^* + \mathbf{H}_g(\mathbf{T}) + \mathbf{H}_T\mathbf{f}_T], \qquad (34a)
\end{aligned}$$

$$\dot{\mathbf{q}}_2 = \mathbf{A}_2^{-1} [\mathbf{\Lambda}_2\mathbf{q}_1 + \mathbf{\Gamma}_3(\mathbf{q}_1)\mathbf{q}_2], \qquad (34b)$$

$$\dot{\mathbf{q}}_a = \mathbf{P}_1\mathbf{q}_1^* - V_\infty\mathbf{P}_2\mathbf{q}_a, \qquad (34c)$$

$$\dot{\mathbf{T}}_v = \mathbf{N}_R(\mathbf{T})\,\mathbf{q}_1, \qquad (34d)$$

$$\dot{\mathbf{r}} = \mathbf{N}_D(\mathbf{T})\,\mathbf{q}_1, \qquad (34e)$$

with the nonlinear terms expressed in terms of operators $\mathbf{\Gamma}$, $\mathbf{N}$ and $\mathbf{H}$ that are linear functions of their respective variables. Therefore only quadratic couplings are present, which will simplify both the numerical solution and the analysis of the nonlinear aircraft dynamics.

# III. System Linearisation and Control Design

## III.A. Open-Loop Linear System Definition

A linearisation of the nonlinear aeroelastic system (34) is made for the purpose of control design. This assumes that a trim solution is found such that $\dot{\mathbf{q}}_1 = \mathbf{0}$, $\dot{\mathbf{q}}_2 = \mathbf{0}$, $\dot{\mathbf{T}} = \mathbf{0}$ and $\dot{\mathbf{q}}_a = \mathbf{0}$. The variables $\mathbf{q}_1$, $\mathbf{q}_2$, $\mathbf{q}_a$ and $\mathbf{T}$ (i.e. excluding the displacement $\mathbf{r}$) are linearised about this equilibrium state, which we will refer to as $\mathbf{q}_0$. This linearisation results in a linear system containing the velocity and force structural modes, aerodynamic modes and nodal rotation variables. Since a direct linearisation on rotational matrices would result in redundant variables, for linearisation purposes it is convenient[24] to introduce the infinitesimal rotation $\mathbf{\Psi}_n(t)$ associated with the $n$-th node of a finite-element discretization of the structure with three degrees of freedom per node, in orientation from trimmed equilibrium condition. The infinitesimal rotation is defined so that $\dot{\mathbf{\Psi}}_n(t) = \boldsymbol{\omega}_n(t)$. Thus the state variable in the linearised system is

$$\mathbf{q}_l = [\ \mathbf{q}_1^\top \quad \mathbf{q}_2^\top \quad \mathbf{q}_a^\top \quad \mathbf{\Psi}^\top\ ]^\top. \qquad (35)$$

We define the linearised state-space aeroelastic system $\mathbf{S}$ to be a continuous, linear, time-invariant system containing states $\mathbf{q}_l$, inputs and outputs. In particular, the system inputs include disturbances $\mathbf{w}_d$ and control actions $\mathbf{u}_c$, whereas the outputs include sensor measurements $\mathbf{y}_m$ and performance outputs $\mathbf{y}_c$. The resulting system $\mathbf{S}$ has in this case the following structure

$$\begin{pmatrix} \dot{\mathbf{q}}_l \\ \mathbf{y}_c \\ \mathbf{y}_m \end{pmatrix} = \begin{pmatrix} \mathbf{S}_A & \mathbf{S}_{B1} & \mathbf{S}_{B2} \\ \mathbf{S}_{C1} & \mathbf{0} & \mathbf{0} \\ \mathbf{S}_{C2} & \mathbf{0} & \mathbf{0} \end{pmatrix} \begin{pmatrix} \mathbf{q}_l \\ \mathbf{w}_d \\ \mathbf{u}_c \end{pmatrix}. \qquad (36)$$

The disturbance inputs in this work are assumed to arise from gusts which affect the system via (32). Linearising (34) with respect to gust strength $\mathbf{w}_d$ gives the matrix $\mathbf{S}_{B1}$ in (36). The gust contribution in the linearisation of Eq. (34a) will be written as

$$\begin{aligned}\mathbf{S}_{B,q1}\mathbf{q}_{1g} := \mathbf{A}_1^{-1}[(&\mathbf{H}_1(\mathbf{q}_{1g}) + \mathbf{H}_{3,d}(\mathbf{q}_{1g})\delta_{d,0})\mathbf{q}_{1,0} \\ &+(\mathbf{H}_1(\mathbf{q}_{1,0}) + V_\infty \mathbf{H}_2(\mathbf{q}_{a,0}) + \mathbf{H}_{3,d}(\mathbf{q}_{1,0})\delta_{d,0})\mathbf{q}_{1g}],\end{aligned} \tag{37}$$

where $\mathbf{q}_{1g} = \mathbf{Q}_{1g}\mathbf{w}_d$ according to Eq. (32) and with $\mathbf{q}_{1,0}$ and $\mathbf{q}_{a,0}$ being trim values of the respective states. Thus it is

$$\mathbf{S}_{B1} = \begin{pmatrix} \mathbf{S}_{B1,q1}\mathbf{Q}_{1g} \\ \mathbf{0} \\ \mathbf{P}_1\mathbf{Q}_{1g} \\ \mathbf{0} \end{pmatrix}. \tag{38}$$

Control actions include control surface deflections through the $\mathbf{H}_3$ term, or by thrust changes through the $\mathbf{f}_T$ term in (34). Linearising (34) with respect to control actions will give rise to $\mathbf{S}_{B2}\mathbf{u}_c$ in (36) where $\mathbf{u}_c$ is the strength of each control action (i.e. its change from trim equilibrium condition). The contribution of the control actions to the linearisation of (34a) is written as

$$\mathbf{S}_{B2,q1}\mathbf{u}_c := \mathbf{A}_1^{-1}(\mathbf{H}_{3,d}(\mathbf{q}_{1,0})\mathbf{q}_{1,0}\delta_d + \mathbf{H}_T\mathbf{f}_T), \tag{39}$$

where $\mathbf{u}_c = [\begin{array}{cc} \boldsymbol{\delta}^\top & \mathbf{f}_T^\top \end{array}]^\top$ and similarly

$$\mathbf{S}_{B2} = \begin{pmatrix} \mathbf{S}_{B2,q1} \\ \mathbf{0} \\ \mathbf{0} \\ \mathbf{0} \end{pmatrix}. \tag{40}$$

Sensor measurements involving either inertial velocities, forces or strains at particular locations are computed by reconstructing the intrinsic variables $\mathbf{x}_1$ and $\mathbf{x}_2$ from the state variables $\mathbf{q}_1$ and $\mathbf{q}_2$ using (2). The collection of such measurements will be referred as $\mathbf{y}_m$ in (36) and in this work,

$$\mathbf{y}_m = \begin{pmatrix} \mathbf{x}_{1,n} \\ \mathbf{x}_{2,n} \end{pmatrix}, \tag{41}$$

where $n$ is the list of node indices at which the measurements are taken. Equation (2) represents a linear relation between $\mathbf{x}$ and $\mathbf{q}$ and can be rewritten to give rise to the measurement matrix $\mathbf{S}_{C2}$. The formulation of the performance output is similar to sensor measurements, but can contain any linear combination of states or inputs to suit the requirement of control design. This would similarly produce $\mathbf{S}_{C1}$ and the performance outputs $\mathbf{y}_c$ in (36).

### III.B. $\mathcal{H}_\infty$ Control Design

The standard $\mathcal{H}_\infty$ control problem is defined on the state-space system $\mathbf{S}$ with the goal of designing an internally stabilising controller of the form

$$\begin{pmatrix} \dot{\mathbf{z}} \\ \mathbf{u}_c \end{pmatrix} = \mathbf{K} \begin{pmatrix} \mathbf{z} \\ \mathbf{y}_m \end{pmatrix}. \tag{42}$$

This represents a control law that uses the measurements $\mathbf{y}_m$ to generate a control action $\mathbf{u}_c$ whose goal is to minimise the $\mathcal{H}_\infty$ norm of the transfer function from the disturbance signal $\mathbf{w}_d$ to the performance output $\mathbf{y}_c$ in (36).

The linearised state-space system (36) has zero feed-through from any of the inputs or disturbances to either performance outputs or measurements. In order to make the control synthesis problem well-posed, additional measurement noise, $\mathbf{w}_m$, and a performance output on the control actions, $\mathbf{y}_{cu}$, are included using diagonal weighting matrices $\mathbf{W}_m$ and $\mathbf{W}_u$. Additional diagonal matrices $\mathbf{W}_d$ and $\mathbf{W}_s$ are used to weight the disturbance and state measurement signals respectively. This results in an augmented state-space system given by

$$\begin{pmatrix} \dot{\mathbf{q}}_l \\ \begin{pmatrix} \mathbf{y}_c \\ \mathbf{y}_{cu} \end{pmatrix} \\ \mathbf{y}_m \end{pmatrix} = \begin{pmatrix} \mathbf{S}_A & \begin{pmatrix} \mathbf{W}_d\mathbf{S}_{B1} & \mathbf{0} \end{pmatrix} & \mathbf{S}_{B2} \\ \begin{pmatrix} \mathbf{W}_s\mathbf{S}_{C1} \\ \mathbf{0} \end{pmatrix} & \begin{pmatrix} \mathbf{0} & \mathbf{0} \\ \mathbf{0} & \mathbf{0} \end{pmatrix} & \begin{pmatrix} \mathbf{0} \\ \mathbf{W}_u \end{pmatrix} \\ \mathbf{S}_{C2} & \begin{pmatrix} \mathbf{0} & \mathbf{W}_m \end{pmatrix} & \mathbf{0} \end{pmatrix} \begin{pmatrix} \mathbf{q}_l \\ \begin{pmatrix} \mathbf{w}_d \\ \mathbf{w}_m \end{pmatrix} \\ \mathbf{u}_c \end{pmatrix}. \tag{43}$$

Note that in the mixed-sensitivity $\mathcal{H}_\infty$ synthesis used in this work, the weighting given by the $\mathbf{W}$ matrices has been replaced by frequency-dependent transfer functions. This further modifies the $\mathbf{S}_A$, $\mathbf{S}_{B2}$ and $\mathbf{S}_{C2}$ matrices by augmenting the system states. For example, the contribution from $\mathbf{W}_u$ is replaced by

$$\begin{pmatrix} \dot{\mathbf{z}}_m \\ \mathbf{y}_{cm} \end{pmatrix} = \begin{pmatrix} \mathbf{W}_{uA} & \mathbf{W}_{uB} \\ \mathbf{W}_{uC} & \mathbf{W}_{uD} \end{pmatrix} \begin{pmatrix} \mathbf{z}_m \\ \mathbf{w}_m \end{pmatrix} \tag{44}$$

and $\mathbf{z}_m$ will be the additional system states that arises from the state-space weighting function. The state-space system (43) now represents a well-posed problem for $\mathcal{H}_\infty$ control synthesis.[25] Note that for the aeroservoelastic systems that we intend to study the number of states are typically between $10^3$ and $10^4$. Consequently, balanced model reduction will first be applied to reduce the system dimensions before $\mathcal{H}_\infty$ controller synthesis.

The robust control toolbox in MATLAB R2015a is used for model reduction and control. The balanced realisation (*balreal*) and model order reduction (*modred*) commands are applied on the state-space system (36) to reduce the system to a given number of states. Weighting transfer functions $\mathbf{W}_m$, $\mathbf{W}_u$, $\mathbf{W}_d$ and $\mathbf{W}_s$ are then specified and lastly the $\mathcal{H}_\infty$ synthesis routine (*hinfsyn*) is used to synthesise an $\mathcal{H}_\infty$ controller based on the weighted, reduced-order system. Control saturation has not been included and tuning of gains was carried out to achieve the desired magnitude of control action against the anticipated disturbance. This is done by applying full-control authority to a gust strength that is just below inducing an angle of attack that causes stall on any part of the wing.

# IV. Aeroelastic Simulation Results

We demonstrate the fully coupled dynamic aeroelastic implementation of the framework in this section. A linear test case concerning flutter on a cantilever wing will be investigated first and compared to published data to verify the implementation of the unsteady aerodynamic model. Subsequently a model of a full aircraft with a flexible, flying wing configuration first described by Patil *et al.*[23] will be constructed. This is to demonstrate the extraction of modal information from nonlinear time-domain simulations using the current framework. Trim and dynamic stability analysis will be carried out on a number of uncontrolled (open-loop) configurations, then an $\mathcal{H}_\infty$ control design with the objective being dynamic stabilisation will also be demonstrated on the system, followed by a closed-loop simulation of the flight dynamics of the aircraft. These results will finally be used to identify dominant contributions to observed nonlinear behaviour by taking advantage of the modal formulation.

## IV.A. Linear Stability Analysis of the Goland Wing

The Goland wing model[26] is first used to verify the coupled structural and aerodynamic model. The Goland wing is a low aspect ratio wing in a cantilever configuration and is a well-studied benchmark numerical test case for aeroelastic simulations based on beam elements. Its properties can be found in Table 1.

| | | | |
|---|---|---|---|
| Chord, $2b$ | 1.8288m | Mass per unit length, $\rho_m A$ | 35.71kg/m |
| Semi-span, $L$ | 6.096m | Moment of inertia around e.a., $\rho_m I_1$ | 8.64 kg·m |
| Elastic axis (from l.e.) | $0.66b$ | Torsional stiffness, $GJ$ | $0.99\times10^6$N·$m^2$ |
| C.G. (from l.e.) | $0.86b$ | Bending stiffness, $EI_2$ | $9.77\times10^6$N·$m^2$ |

**Table 1. Relevant properties of the Goland wing**

The forward flight velocity is included in the model by prescribing a forward rigid-body velocity mode $\mathbf{q}_1$ in (34), then the steady-state aerodynamic lag terms $\mathbf{q}_a$ in (34), which are non-zero due to the forward velocity, are solved (the simplicity of the case makes this step trivial). The airspeed at which flutter occurs on the Goland wing is computed by a linearisation of the dynamics over a range of increasing airspeeds where the appearance of an unstable eigenvalue in the linearised dynamics indicates that flutter has occurred (this is sometimes referred to as the p-method). After convergence, the current study uses 11 coupled bending/torsion modes and 1 axial mode which produced the results shown in Table 2. These match well with previous studies using 2D aerodynamic approximations, whereas 3D aerodynamic methods such as UVLM more accurately reflect tip effects which have a noticeable impact on the computed flutter speed. It is also worth noting that Sotoudeh's model accounts for apparent mass effects, which results in the small difference to the current result. However, in this case differences due to modelling the tip effect are much more significant.

| Author | Model | $V_f$, $ms^{-1}$ | $\omega_f$, $rad\,s^{-1}$ |
|---|---|---|---|
| Current | Intrinsic / 2D aero (Modal) | 139 | 70.0 |
| Sotoudeh et al[27] | Intrinsic / 2D aero (FD) | 137 | 70.1 |
| Wang et al[6] | Intrinsic / UVLM | 164 | - |
| Murua et al[28] | Displacement / UVLM | 165 | 69 |

**Table 2. Flutter velocity and frequency for the Goland wing at** $\rho_\infty = 1.02\,kg\,m^{-3}$

## IV.B. Verification on a High Aspect Ratio Flying Wing

### *IV.B.1. Test case description*

A nonlinear aeroelastic test case in the form of a very flexible airframe is considered next for the purpose of demonstrating control design and closed-loop nonlinear dynamic simulation, as well as illustrating the advantages of the method in obtaining modal information from the simulation. This test case will also verify the flexible dynamic models with established results. The aircraft is the 72m-span high-aspect ratio flying wing model created by Patil et al.[23] and subsequently used by Su et al.[8] , which is shown in Figure 3. Its properties are shown in Table 3. The airframe has a flat, straight midsection and an outer section with 10° dihedral. Three vertical fins are placed below the midsection and thrust is provided by five propellers mounted forward of the midsection. The payload is placed in the central pod and is variable between 0 (0 %) and 227 kg (100 %).

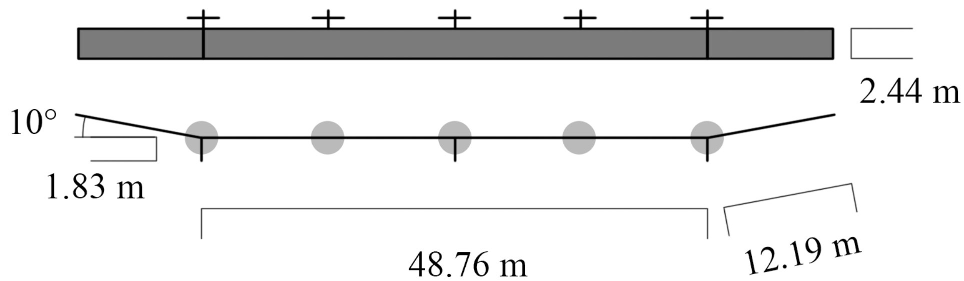


**Figure 3. Geometric configuration of the flying wing.**

| | |
|---|---|
| Elastic/reference axis | 25% chord |
| Aerodynamic centre | 25% chord |
| Centre of gravity | 25% chord |
| $GJ$ | $1.65 \times 10^5 \mathrm{Nm}^2$ |
| $EI_2$ | $1.03 \times 10^6 \mathrm{Nm}^2$ |
| $EI_3$ | $1.24 \times 10^7 \mathrm{Nm}^2$ |
| $m$ | 8.93kg/m |
| $I_{11}$ | 4.15 kg m |
| $I_{22}$ | 0.69 kg m |
| $I_{33}$ | 3.46 kg m |
| Wing $c_{l\alpha}$ | $2\pi$ |
| Wing $c_{l\delta}$ | 1 |
| Wing $c_{d0}$ | 0.01 |
| Wing $c_{m0}$ | 0.025 |
| Wing $c_{m\delta}$ | -0.25 |
| Pod $c_{l\alpha}$ | 5 |
| Pod $c_{d0}$ | 0.02 |
| Pod $c_{m0}$ | 0 |

**Table 3. Relevant properties of the flying wing.**[8]

The structural model of the aircraft is created using a separate, in-house, finite-element composite beam solver,[29] with 40 elements for each side of the central section, 20 elements for the outer section and 1 rigid element each for each of the 3 fins under the wing. Eigenvalue analysis was then performed on the structure, obtaining the structural modes in the intrinsic formulation defined on the 124 nodes on the airframe using the procedure outlined in Wang *et al.*[30] The payload is considered part of the model, thus varying the payload requires re-computing the modes. It is worth noting that Moulin *et al.*[31] demonstrated a method in which this is avoided but this is not investigated here. The natural modes and frequency information leads to the $\mathbf{A}$, $\mathbf{\Lambda}$ matrices and $\mathbf{\Gamma}$ coefficients in (34). Additional definitions of aerofoil coefficients in Table 3 lead to the aerodynamic influence coefficients $\mathbf{H}$.

The lowest frequency elastic mode shapes in velocity vector ($\boldsymbol{\phi}_1|_{123}$) and the sectional moment vectors ($\boldsymbol{\phi}_2|_{456}$) in the corresponding force modes are shown in Figure 4. The angular velocity and sectional force vectors are not shown. Note here that the velocity vector, when plotted in global coordinates, scales directly with displacement vectors, while the sign of force and moment are dependent on the definition of the beam direction.

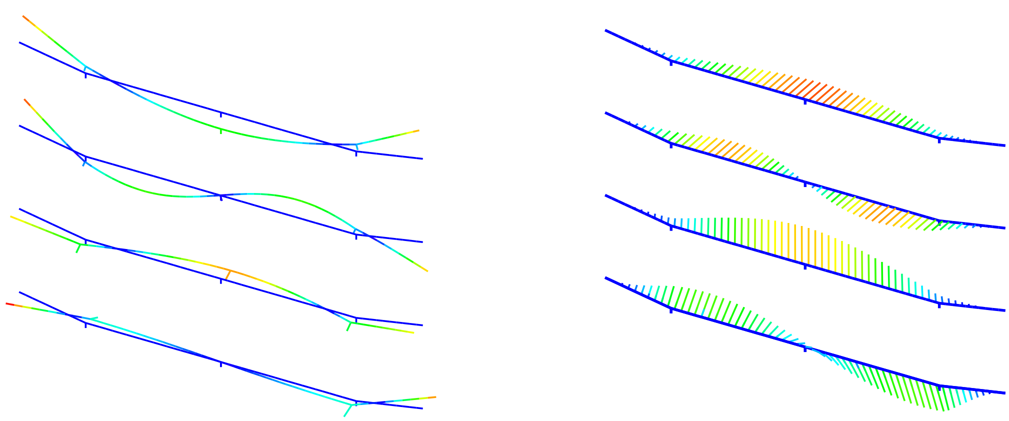

(a) Velocity mode vector

(b) Moment mode vector

**Figure 4. Field plots of local sectional velocity and sectional moment vectors for the first four structural modes of the 0-payload airframe. They correspond to (from above) symmetric out-of-plane bending, antisymmetric out-of-plane bending, symmetric in-plane bending and antisymmetric in-plane bending.**

In this work we are interested in the symmetric response of the airframe and thus define two possible *symmetric* control actions available on this flying wing for control design and closed-loop flight: a simultaneous flap deflection by a fixed angle on the entire wing $\delta$ and a differential flap deflection $\delta_D$ by deflecting the flaps on the outboard section (the section with dihedral) down and the inboard flaps up. The differential flap input is designed to provide improved control on the degree of bending exhibited on the wing. For trimming the airframe however, only the simultaneous flap control is used, together total engine thrust, while the differential flap control input is set to zero.

### *IV.B.2. Trim Solution, Stability and Open-Loop Response Verification*

The vehicle is flown at 12.2 m/s at sea level[23] and its trim condition is computed for various central pod payloads and for both the rigid airframe and the fully flexible airframe. The rigid case uses six rigid-body velocity modes ($\mathbf{q}_1$), whereas the flexible case uses the first 294 symmetric flexible structural velocity modes together with the six rigid-body velocity modes. It was found that such a number of modes is required for convergence of the flexible, large-deformation trim solution, and it is linked to the minimum spanwise wavelength appearing in the deformed shape, which is only provided by the higher mode shapes. However, it will be seen that linear dynamic analysis and control design around this reference condition require far fewer number of states. The total number of aerodynamic states ($\mathbf{q}_a$) is equal to the total number of velocity modes, multiplied by the total number of rational function approximation terms ($N_{AE}$) in Wagner's function. As throughout this work $N_{AE} = 2$, the rigid model contains 18 states in total (6 rigid body velocities and 12 associated aerodynamic modes) and the flexible model contains 1194 structural and aerodynamic modes ($N_M =$ 294 velocity and force modes, 6 rigid body and 600 associated aerodynamic modes). Both models are augmented with states associated with displacements $\mathbf{r}$ and rotations $\mathbf{T}$ at the finite-element nodes. The aerodynamic states are included for trim as the instantaneous aerodynamic forces only provide a portion (exactly one-half in the formulation) of the steady-state lift (through $\mathbf{H}_1$ terms in (34)), the other part comes from the $\mathbf{H}_2$ and $\mathbf{q}_a$ terms describing the unsteady aerodynamic forces and are non-zero at steady-state due to the choice of aerodynamic formulation.

The process of trimming the airframe includes first prescribing a angle of attack for the vehicle, then computing the aerodynamic loads on a starting configuration (zero deformation) under such conditions. These aerodynamic forces are then regarded as constant forces applied on a non-deforming airframe, and the correct amount of structural deformation, thrust force, flap deflection and gravity (variable in strength for the purpose of trim) are computed to exactly balance this aerodynamic force and keep the aircraft flying level at the fixed velocity. Next, the airframe is allowed to deform until equilibrium under the fixed aerodynamic force and lastly the aerodynamic forces are updated under the new configuration and the entire process iterated. By iterating on the angle of attack through the method of bisection, the trim condition is computed.

The trim angle of attack (computed at the centre node of the airframe), thrust and flap deflection for varying centre pod payload is shown in Figure 5, with comparison against Su[8] and Patil.[23] As discussed in Section II.B, minor differences in the detail of the small-angle approximation used to describe the aerodynamic forces on the aerofoil may have contributed to the small differences seen in the results on larger payload values but the overall agreement is excellent. The structural deformations at the trim conditions of the six different payloads are shown in Figure 6.

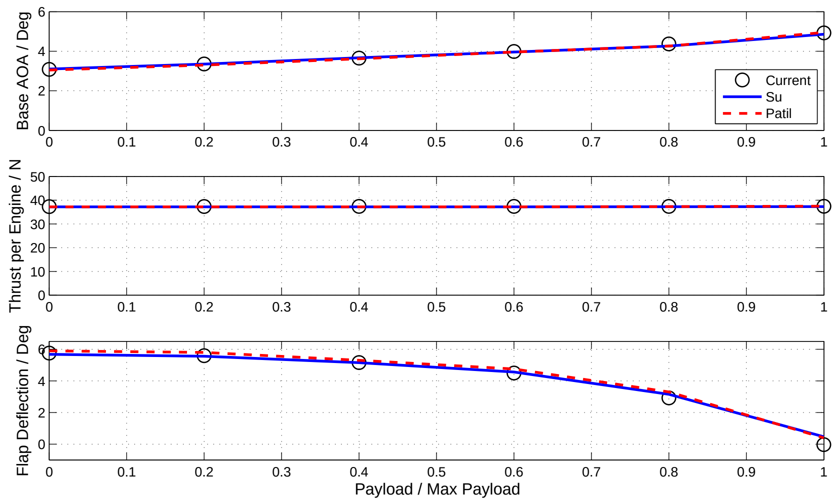


**Figure 5. Angle of attack, engine thrust and flap deflection at trim condition for payload varying from 0 to 227 kg, compared against previous results by Su[8] and Patil[23]**

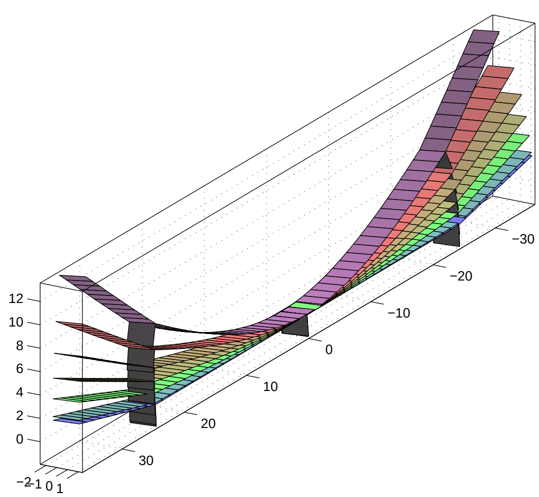

**Figure 6. Static deformation at trim condition compared to undeformed shape (bottom) for increasing payloads of (0,20%,40%,60%,80%,100%), with the 100% configuration being on the top.**

Subsequently a linearized eigenvalue analysis of the system around the trim configuration is performed for each payload of the rigid/flexible case (Figure 7). Comparison is also made here for the phugoid eigenvalue between the current method and previous works by Su et al.[8] and Patil et al.[23] .

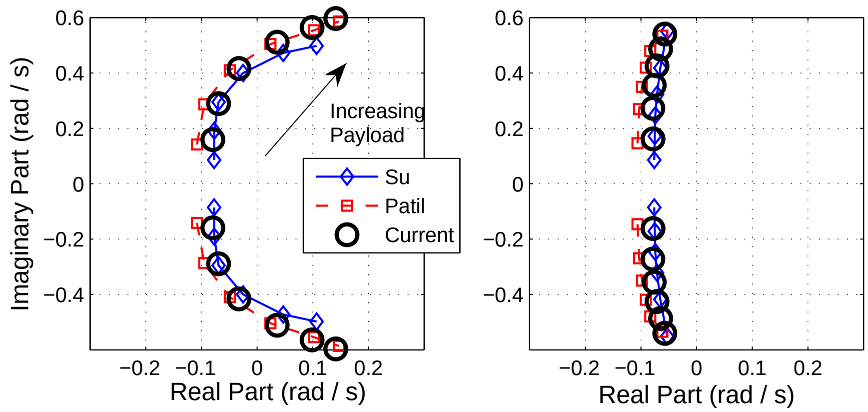


**Figure 7. Root locus of the phugoid mode of the flexible (left) and rigid (right) airframe computed with payloads varying from 0 to 100%, compared against previous results by Su[8] and Patil[23]**

Here the importance of flexibility on the dynamic stability of this airframe is highlighted with the phugoid mode becoming unstable in the flexible case after 51% payload, while in the rigid airframe the phugoid mode is always stable. A decreased level of stability in this model is associated with an increased bending deformation on the wing, as shown in Figure 6. The phugoid frequency and damping for different payloads matches very well with Patil's results (while Su's frequency tends to be lower). However the damping of the phugoid mode lies closer to Su's results. Given the difference between the two referenced results, the current result is deemed to be in good agreement with them. The stability boundary of 51% payload again agrees well with both Patil's (51%) and Su's (61%).

Nonlinear dynamic simulation is performed using the trimmed airframe model of 100% payload with an excitation caused by transient, simultaneous flap deflections of the form shown in Figure 8. This test case has previously been investigated by Patil[23] and the resulting response and comparison is shown in Figure 9. It is seen that the results compare very well and the small differences can be primarily attributed to the use of small-angle approximations and the assumption of constant freestream velocity at any given time. As the setup is dynamically unstable, the airframe reaches large angles of attack after 20 seconds. Therefore the response after this time exceeded the operating range for the assumptions made in the numerical model to be valid, since neither model includes stall. Snapshots of the instantaneous shape of the aircraft, as it is subjected to the simulated input, are shown

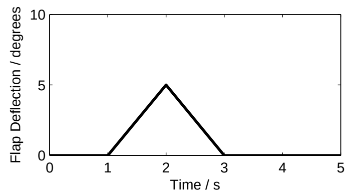


**Figure 8. The initial flap input on the open-loop airframe test case.**

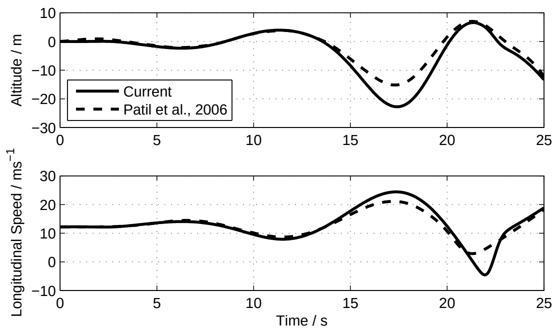


**Figure 9. Dynamic open-loop response to the flap deflection of Figure 8.**

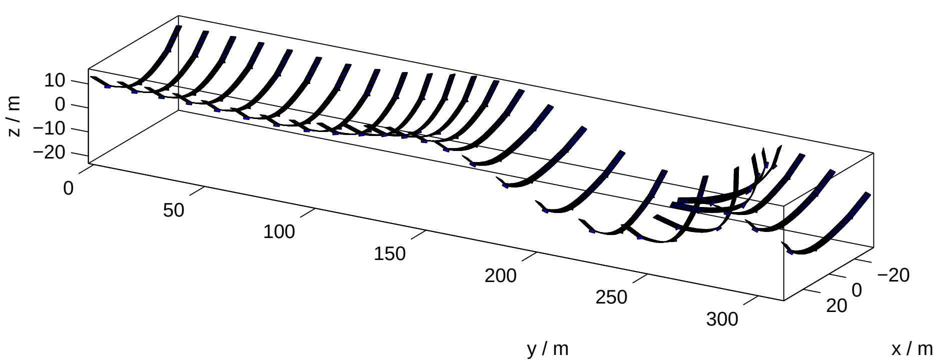


**Figure 10. 25-second flight of the flying wing after being subjected to the flap deflection of Figure 8.**

in Figure 10.

### IV.C. Control Design on Flying Wing System

Here we will describe the process of linearisation and control design on the dynamically unstable open-loop 100%-payload model using the process outlined in Section III.B, with the objective being stabilisation and gust load alleviation on the full-payload system. The aeroelastic formulation of the system (34) makes linearisation around a trim equilibrium easy to implement. In addition, the linearised equations in the current modal formulation still describe the dynamics in terms of the structural modes $\mathbf{q}$ and will provide some insight into the interplay of aeroelastic interactions between different modes.

We first define the input and output of the dynamic system in order to define the state-space description on which we perform the control design. The control action input ($\mathbf{u}_c$ in (36)) are the four controls (symmetric and differential flap and thrust) described in Section III.A written in state-space form using the method in Section III.A. The disturbance input ($\mathbf{w}_d$ in (36)) includes two channels. The first being a spanwise $1 - \cos$ vertical force distribution, centred on the midpoint of the airframe, in order to simulate a worst-case gust distribution that causes bending of the airframe; the second being a constant spanwise force distribution designed to simulate a gust without spatial variation. Four measurements ($\mathbf{y}_m$ in (36)) are defined, all taken at the midpoint of the airframe, while also serving as the performance output ($\mathbf{y}_c$ in (36)) with the appropriate weightings to tune the resulting closed-loop response. They include local velocities in the chordwise and normal directions, local out-of-plane bending stress measurements and pitching rotation. These four measurements are designed to provide information both on the flight dynamics and the deformation of the airframe. These definitions of inputs and outputs thus yield a state-space description with $4 + 2$ inputs including controls and disturbances and $4 + 4$ outputs including performance outputs and measurements.

The 100% payload model is linearised according to the method described in Section III.A. The 1566-state linearised system is then reduced by balanced reduction prior to control design. Figure 11 shows the Hankel singular values for the stable states (i.e. excluding the unstable pair corresponding to the phugoid) in the linearised aeroelastic system. From the singular value plot it can be seen that only a small number of states contribute significantly to the overall input-output behaviour of the system. Figure 12 is a comparison of the Bode plots of full- and reduced-order open loop systems. Both balanced truncation, where modes are simply removed, and residualisation, where modes that are removed act instead as feed-through to preserve DC gain,[32] are compared. It can be seen that the reduced-order models from both balanced truncation and residualisation with only 20 states reproduces the dynamics of the original system at frequencies with a high accuracy at frequencies below

2 rad/s which is appropriate for the slow dynamics of the aircraft under consideration.

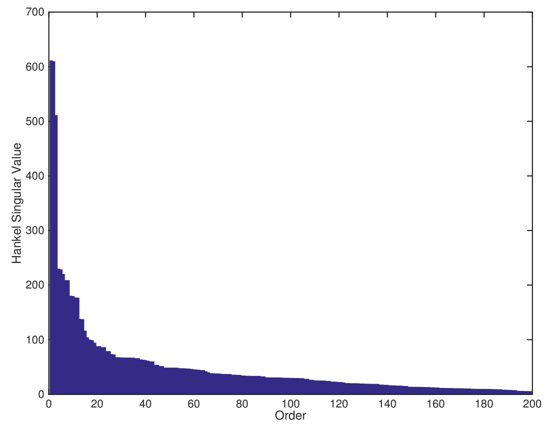


**Figure 11. Hankel singular values in the linearised aeroelastic system (100% payload). Only the largest contributions are shown, while the pair of unstable states has been excluded.**

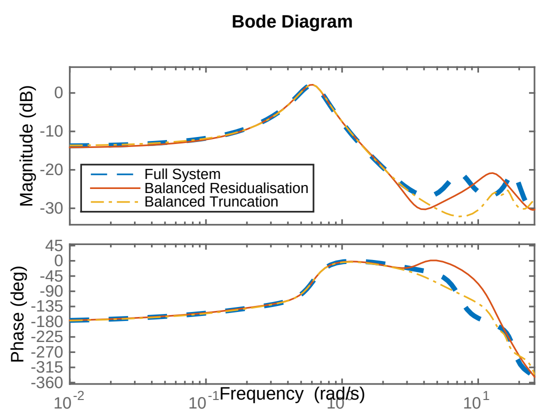


**Figure 12. Bode plot of open-loop full- and reduced-order system with 20 states from symmetric flap input to change in angle of attack (100% payload case).**

The full system is thus reduced by balanced model reduction and a 20-state system is obtained. Frequency-based weightings on each part of the performance outputs are applied as described in Section III.B. The controller is designed so that it applies close to the maximum possible control action below the control saturation range for each control channel (a range of $\pm 10$ degrees for symmetric and differential flap), for the aerodynamic load corresponding to the maximum admissible gust encounter, i.e. the maximum possible gust without instantly stalling the aircraft. As the aircraft travels at 12.2 m/s, the load corresponding to a maximum vertical gust of 5 m/s is considered a major event to test the controllability of the vehicle and is used as a worst-case scenario. The low-frequency poles of the closed-loop system are shown in Figure 13. It can be seen in the figure that the unstable phugoid mode in both reduced- and full-order system is moved to the LHS half-plane, indicating the controller achieves stabilisation.

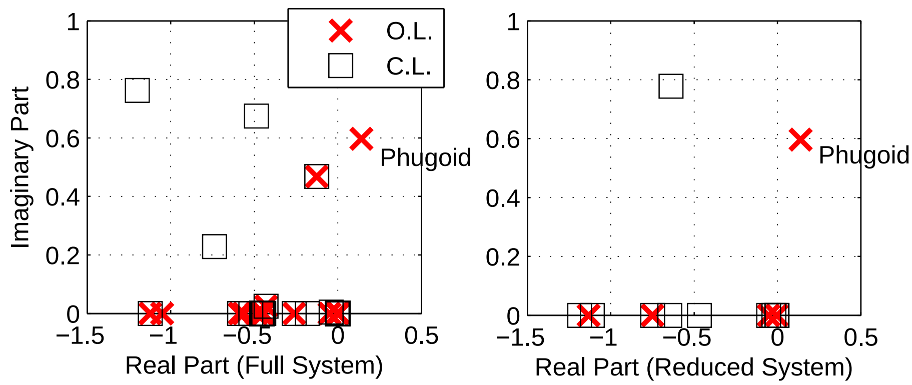


**Figure 13. Low-frequency poles in the flying-wing testcase, showing the poles in the full- and reduced-order system, both in open loop and in closed loop. The open-loop pole on the full-state system that is not moved by the controller is an antisymmetric mode.**

## IV.D. Closed-Loop Flight of Flying Wing

Finally, we apply the control system developed above to the full nonlinear model of the full-payload flying wing. The excitation used is a DARPA gust, which is a transient vertical gust with a spanwise distribution designed to excite symmetric wing bending. The vertical gust velocity $\mathbf{v}_{g,3}$ at a location $\mathbf{u}$ is defined as

$$\mathbf{v}_{g,3} = -\frac{1}{2}(1 - \cos(2\pi t/t_g))\frac{1}{2}\cos(\pi(u_2 - u_{2,0})/L_y)u_g \tag{45}$$

in the interval $0 < t < t_g$ and $\mathbf{v}_{g,3} = 0$ for $t \geq t_g$. Here $u_g$ indicates the strength of the gust, $t_g$ the gust duration and $u_{2,0}$ the current location of the reference point which for the flying wing it is defined as the wing's mid point. The $y$-component of $\mathbf{u}$ is denoted $u_2$, assuming a global coordinate in which the aircraft flies in the $x$-direction and the $z$-axis points up. $L_y$ is the characteristic size of the spatial variation of the gust, for this problem a value of 72m is used.

Figures 14 and 15 illustrate the responses and control actions applied for the airframe experiencing the above-mentioned gust starting at $t$=0, including changes in root bending moment $M_2$, (body-fixed) forward and vertical velocities $v_2$ and $v_3$, as well as the change in pitching angle $\Psi_1$, all measured at the mid-span, for variable gust durations and a fixed gust strength of 0.2m/s. The closed-loop simulations confirm that the controller stabilises the open-loop unstable aeroelastic system using control actions that are well within saturation range. Figures 16 and 17 illustrate the response for a fixed gust duration between 0.5s and strengths from 0.2 and 2 $m/s$, normalised by the gust strength. In these two figures, the response to larger gusts shows differences to that of smaller gusts, namely the wing experiences the maximum deviation in velocity and pitch for considerably longer and illustrating the geometrically nonlinear effects observed on larger deflections. In all cases the controller applies almost no control action to the engine thrust (whose magnitude is below $10^{-4}$ N), the engine thrust is thus not shown. It is also interesting to note that the controller applies almost opposite inputs to simultaneous and differential flap deflections, implying that the outboard flaps are deflected much more than the inboard ones. In all cases the flap deflections are well within the saturation range of 10° each side.

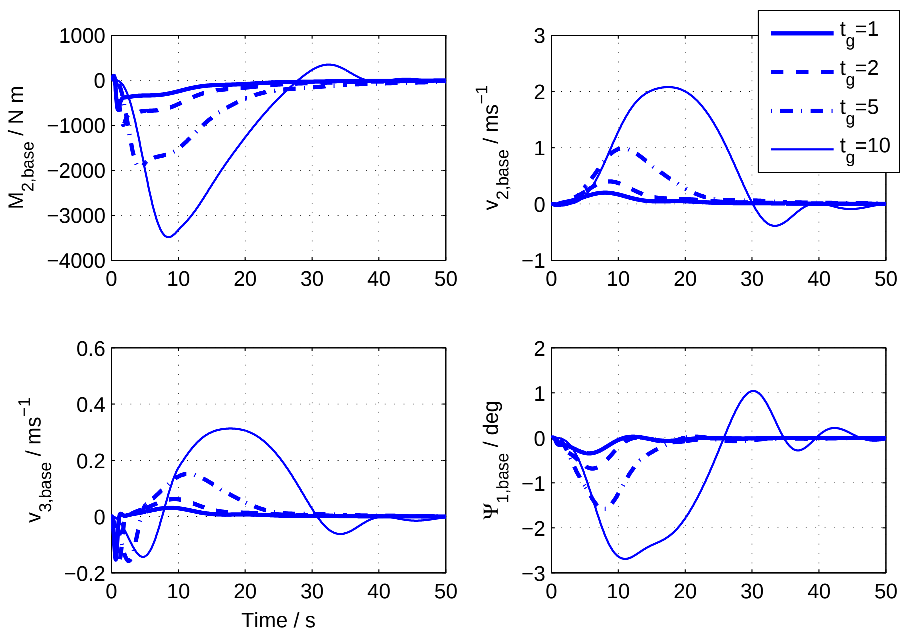


**Figure 14. Airframe responses for different DARPA gust durations at a maximum gust strength of 0.2m/s.**

However, the simulations also show that if the closed-loop system experiences a gust with both a long length and a high strength, the geometrically nonlinear effects eventually render the system unstable, showing the limited authority that this particular controller has on the nonlinear system. This is demonstrated with a maximum gust strength of 2 m/s and a duration of 5s in Figures 18(a) and 18(b) where an initial increase in dihedral due to the gust can be seen clearly and the airframe then enters a divergent dive. It is worth noting the fact that the linear trim results also associate a higher dihedral with a less stable phugoid mode. As part of the performance output, the controller will always try to correct the change in dihedral to remove any associated change in the measured root bending moment. However

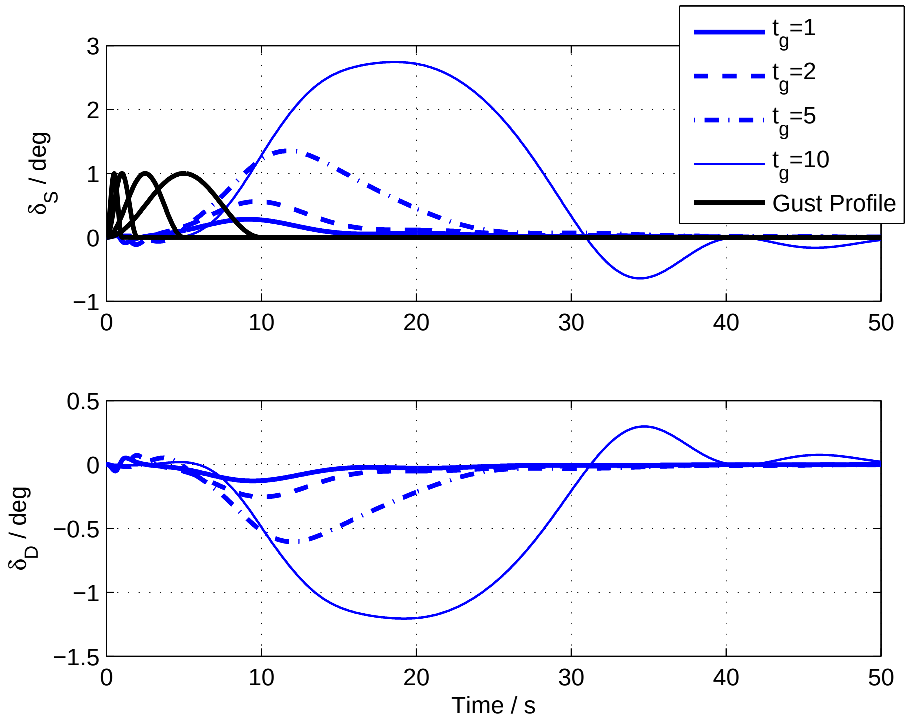


**Figure 15. Control actions for different DARPA gust durations at a maximum gust strength of 0.2m/s. Also plotted is the variation of gust velocity with time. Here 'S' indicates simultaneous inboard and outboard control actions while 'D' indicates differential actions.**

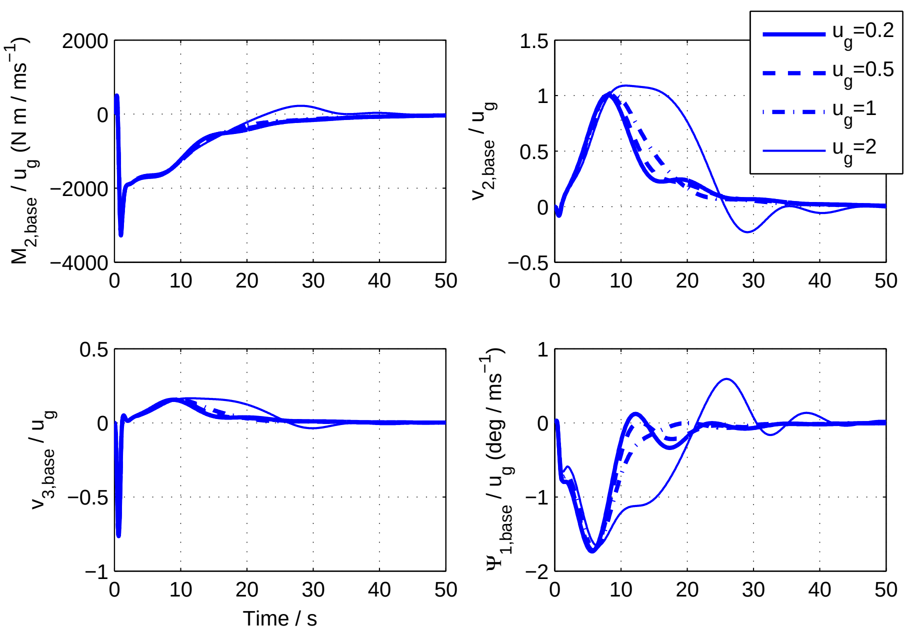


**Figure 16. Airframe responses for different DARPA gust strengths at a total gust duration of 0.5s. Normalised with gust strength $u_g$ in m/s.**

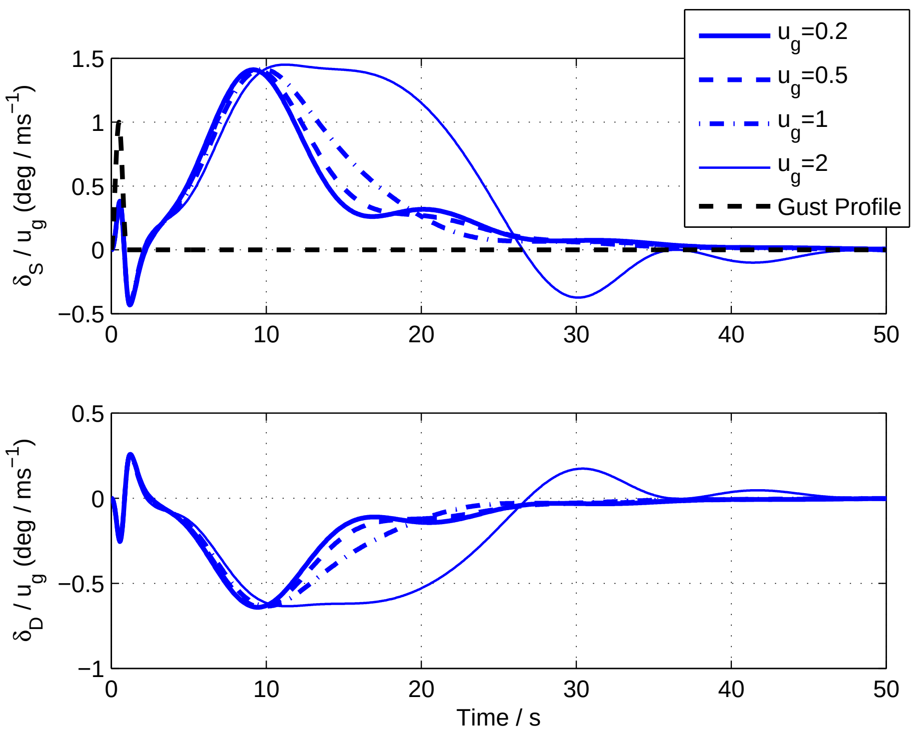


**Figure 17. Control actions for different DARPA gust strengths at a total gust duration of 0.5s. Units in degrees and normalised with gust strength $u_g$ in m/s. Also plotted is the variation of gust velocity with time. Here 'S' indicates simultaneous inboard and outboard control actions while 'D' indicates differential control surface actions.**

in this case it is not achieved fast enough before the system, now nonlinearly closed-loop unstable, enters a dive. Figure 19 illustrates the range of gust intensity and length in which the response is stable to the chosen gust input, a boundary between gust excitations resulting in stable and unstable responses can be seen in the figure.

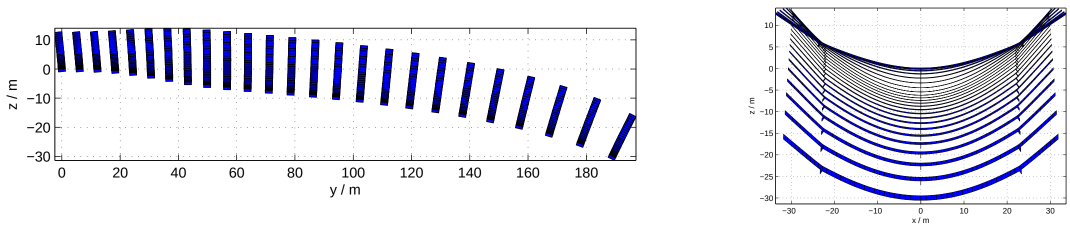


(a) Side view (b) Front view

**Figure 18. Divergent response to a DARPA gust with maximum strength of 2 m/s and a duration of 5s.**

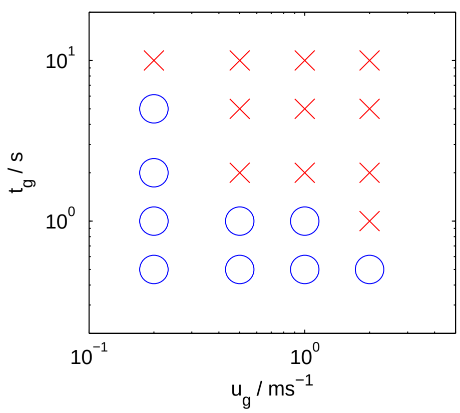


**Figure 19. Stability boundary in the nonlinear response to DARPA gusts of varying lengths $t_g$ and intensities $u_g$. Circle indicates eventual return to trim conditions whereas cross indicates a divergent response.**

Using the closed-loop gust response simulation data, we further identify the contributions of each structural state to the observed dynamics. A major advantage of the current aeroelastic formulation is that the modal contributions are primary variables in the model and both their linear and nonlinear components can be analysed easily. Figure 20 shows the modal amplitudes of the two most-excited states for various gust strengths $u_g = 0.2$ to 2 m/s and at a gust duration of $t_g = 1$s. These are the first mode in sectional forces $q_{27}$, which corresponds to the first structural bending mode, and the forward velocity rigid-body mode, $q_{12}$. As discussed in Section II.A, the intrinsic formulation does not implicitly make distinctions between structural and rigid-body velocities and in this section we number the *symmetric* elastic structural modes starting from $q_{17}$ and $q_{27}$, with the 6 preceding modes being rigid-body. Anti-symmetric structural modes are not included in the numbering scheme. As above, the responses shown in the figure are normalised with the gust strength $u_g$, which highlights the effect of nonlinearity on the time-domain response. Figure 21 shows other significant modal contributions to the resulting response. However, nonlinear effects are not significant in these modes. As in Section II.A, the modes have been normalised with energy, this shows that the response is dominated by the first bending and forward flight rigid-body mode, that are also dominant contributions to the phugoid mode that was already seen to be the most-excited motion by the DARPA gust for this aircraft. This is further confirmed by listing the change in the individual energy contributions to the response, $\frac{1}{2}q_{1j}^2$ and $\frac{1}{2}q_{2j}^2$, relative to the trim condition (the derivation of the energy is made in a previous paper[19]). The r.m.s. value of the contribution is shown in Table 4 for the case of $u_g = 2$ m/s (largest strength) and $t_g = 1$ s (shortest duration). As seen in the table, the contributions from the first bending mode in velocity and force, i.e. $q_{17}$ and $q_{27}$, and the forward flight rigid-body mode $q_{12}$, are overwhelmingly large in comparison to that from the others. This is even more significant as for $u_g = 2$ m/s significant nonlinearity is already observed.

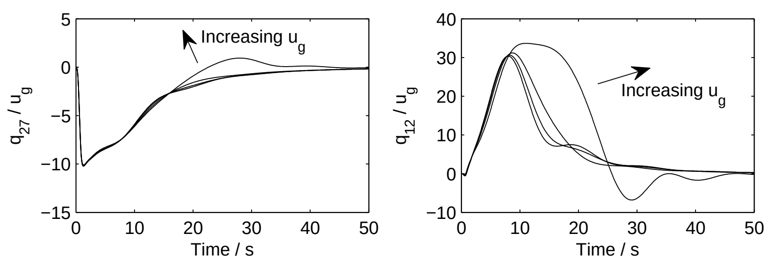


**Figure 20. Time-series of the modal amplitudes of first bending strain mode $q_{27}$ and forward rigid-body velocity mode $q_{12}$, normalised by $u_g$ for $u_g = 0.2$ to 2 m/s at $t_g = 1$ s.**

Taking advantage of the formulation, we also directly analyse the individual nonlinear terms by monitoring their respective contributions to $\dot{\mathbf{q}}$. For $u_g = 2$ m/s and $t_g = 1$ s where it is seen that significant nonlinearities are encountered. Table 5 illustrates the r.m.s. measure of the nonlinear contributions to the largest $\dot{\mathbf{q}}$ as observed from Table 4 (first bending velocity $\dot{q}_{17}$, forward rigid-body velocity $\dot{q}_{12}$ and vertical rigid-body velocity $\dot{q}_{13}$) for the duration of the simulation, i.e. those occurring from the nonlinear coupling terms $\mathbf{\Gamma}$ and $\mathbf{H}$ in (34) around the trim equilibrium which deviates from the linearised model. This analysis also shows that almost all the nonlinear contributions observed in the dynamic response arise from the coupling terms involving $q_{17}$, $q_{12}$ and $q_{13}$, that is, bending, forward and normal velocities with the remaining couplings insignificant. An important conclusion to be drawn from this analysis is that potential nonlinear reduced-order models may only need to retain

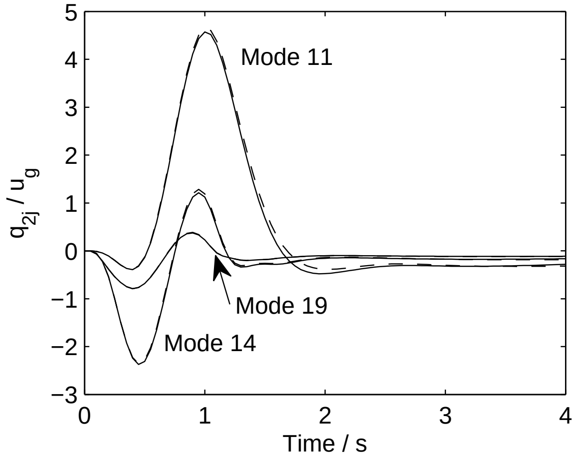


**Figure 21. Time-series of the modal amplitudes of $q_{2j}$ for $j = 11$ (3rd out-of-plane bending), 14 (2nd coupled in-plane), 19 (6th out-of-plane bending). Dashed line corresponds to $u_g = 2$ m/s and solid line corresponds to $u_g = 0.2$ m/s, both at $t_g = 1$ s.**

| Mode Number | Mode Type | $q_{1j}$ Contribution | $q_{2j}$ Contribution |
|---|---|---|---|
| 2 | Forward translation | $2.83\times10^{4}$ | - |
| 3 | Vertical translation | $3.51\times10^{2}$ | - |
| 4 | Pitching rotation | $7.93\times10^{-1}$ | - |
| 7 | 1st out-of-plane bending | $6.25\times10^{1}$ | $2.12\times10^{3}$ |
| 8 | 1st coupled in-plane (type 1) | $< 10^{-6}$ | $< 10^{-6}$ |
| 9 | 2nd out-of-plane bending | $6.22\times10^{-1}$ | $1.23\times10^{0}$ |
| 10 | 1st coupled in-plane (type 2) | $< 10^{-6}$ | $< 10^{-6}$ |
| 11 | 3rd out-of-plane bending | $2.55\times10^{0}$ | $2.57\times10^{1}$ |
| 12 | 1st coupled in-plane (type 3) | $1.47\times10^{-2}$ | $2.36\times10^{0}$ |
| 13 | 4th out-of-plane bending | $< 10^{-6}$ | $< 10^{-6}$ |
| 14 | 2nd coupled in-plane (type 1) | $4.83\times10^{-1}$ | $3.79\times10^{0}$ |
| 15 | 2nd coupled in-plane (type 2) | $< 10^{-6}$ | $< 10^{-6}$ |
| 16 | 5th out-of-plane bending | $3.47\times10^{-3}$ | $1.90\times10^{-1}$ |
| 17 | 2nd coupled in-plane (type 3) | $< 10^{-6}$ | $< 10^{-6}$ |
| 18 | 3rd coupled in-plane (type 1) | $< 10^{-6}$ | $< 10^{-6}$ |
| 19 | 6th out-of-plane bending | $2.85\times10^{-2}$ | $2.28\times10^{-1}$ |
| 20 | 3rd coupled in-plane (type 3) | $4.64\times10^{-4}$ | $2.89\times10^{-1}$ |

**Table 4. RMS energy contributions from each individual mode for $u_g = 2$ m/s and $t_g = 1$ s. Rigid-body (modes 1-6) and *symmetric* structural modes are listed (anti-symmetric structural modes are not included in the numbering scheme), as well as their type. Rigid-body modes 1,5,6 are anti-symmetric and also are not included.**

the nonlinear couplings involving these modes to effectively capture the contributions of the nonlinearity to the dynamics. This exercise also demonstrates that the use of natural structural modes as a basis for both structural and aerodynamic models can lead to a better understanding of the dominant nonlinear couplings in a system.

| NL terms in | $q_{12}q_{12}$ | $q_{12}q_{13}$ | $q_{12}q_{17}$ | $q_{13}q_{13}$ | $q_{13}q_{17}$ | $q_{17}q_{17}$ | $q_{27}q_{27}$ | Other terms |
|---|---|---|---|---|---|---|---|---|
| $\dot{q}_{12}$ | 147.6 | - | - | 16.54 | 0.1248 | 0.0636 | - | 0.2136 |
| $\dot{q}_{13}$ | - | 805.18 | 3.1275 | - | - | 0.000487 | 1.0261 | 8.6127 |
| $\dot{q}_{17}$ | - | 241.02 | 11.32 | - | 0.00163 | $< 10^{-6}$ | 0.4456 | 1.7427 |
| $\dot{q}_{27}$ | - | - | - | - | - | - | - | 1.7922 |

**Table 5. RMS of contribution of nonlinear couplings to individual $\dot{q}$ for the case of $u_g = 2$ m/s and $t_g = 1$ s.**

# V. Conclusions

A nonlinear aeroservoelastic simulation framework in modal coordinates has been developed. The description is based on coupling the intrinsic formulation of geometrically-nonlinear composite beam equations and 2D unsteady aerodynamics at each spanwise location of the lifting surfaces. The degrees of freedom are further projected in the linear normal modes of a reference configuration. This yields a nonlinear aeroelastic description that reduces to conventional linear methods for small wing deflections. For nonlinear problems, the intrinsic description of the dynamics implies that only quadratic terms are required. However, it also requires a much higher number of modes than a linear solution for convergence, as this is linked now not only to the frequency bandwidth of interest, but also to the approximation of the deformed structure using mode shapes.

The implementation has been verified using a cantilever wing and a very flexible aircraft configuration. Numerical simulations have showed that the current framework is able to reproduce nonlinear steady-state and unsteady dynamic responses found in the literature. We have also demonstrated the capacity of this framework to provide linearised models for control design, and the evaluation of controller performance on the fully nonlinear simulation. In particular we have used the model to demonstrate a case where a linear control design fails to stabilise the unstable airframe when it encounters a large disturbance that creates geometrically-nonlinear deformations. In order to further quantify the nonlinearity, we have identified the main contributors to the observed nonlinear behaviour in modal coordinates. Future work will investigate the development of a nonlinear reduced-order model for the problem as a basis for improved control design and performance.

## Acknowledgements

This work is partially funded by the UK Engineering and Physical Sciences Research Council Grant EP/I014683/1 "Nonlinear Flexibility Effects on Flight Dynamics and Control of Next-Generation Aircraft". That support is gratefully acknowledged. All results in this paper are available as open data. Information on access can be found at the website of Imperial's Load Control & Aeroelastics laboratory (http://www.imperial.ac.uk/aeroelastics/software).


## References


[1]Cesnik, C. E., Palacios, R., and Reichenbach, E. Y., "Reexamined Structural Design Procedures for Very Flexible Aircraft," *Journal of Aircraft*, Vol. 51, No. 5, 2014, pp. 1580–1591.

[2]Drela, M., "Integrated simulation model for preliminary aerodynamic, structural, and control-law design of aircraft," *$40^{th}$ Structures, Structural Dynamics and Materials Conference*, St. Louis, Missouri, USA, April 1999, pp. 1644–1656, AIAA Paper No. 1999-1394.

[3]Meirovitch, L. and Tuzcu, I., "Unified theory for the dynamics and control of maneuvering flexible aircraft," *AIAA Journal*, Vol. 42, No. 4, 2004, pp. 714–727.

[4]Zhao, Z. and Ren, G., "Multibody dynamic approach of flight dynamics and nonlinear aeroelasticity of flexible aircraft," *AIAA Journal*, Vol. 49, No. 1, 2011, pp. 41–54.

[5]Murua, J., Palacios, R., and Graham, J. M. R., "Applications of the unsteady vortex-lattice method in aircraft aeroelasticity and flight dynamics," *Progress in Aerospace Sciences*, Vol. 55, Nov. 2012, pp. 46–72.

[6]Wang, Z., Chen, P. C., Liu, D. D., and Mook, D. T., "Nonlinear-aerodynamics/nonlinear-structure interaction methodology for a high-altitude long-endurance wing," *Journal of Aircraft*, Vol. 47, No. 2, 2010, pp. 556–566.

[7]Patil, M. J., Hodges, D. H., and Cesnik, C. E., "Nonlinear aeroelasticity and flight dynamics of high-altitude long-endurance aircraft," *Journal of Aircraft*, Vol. 38, No. 1, 2001, pp. 88–94.

[8]Su, W. and S. Cesnik, C. E., "Dynamic response of highly flexible flying wings," *AIAA Journal*, Vol. 49, No. 2, 2011, pp. 324–339.

[9]Palacios, R., Murua, J., and Cook, R. G., "Structural and Aerodynamic Models in Nonlinear Flight Dynamics of Very Flexible Aircraft," *AIAA Journal*, Vol. 48, No. 11, 2010, pp. 2648–2659.

[10]Mignolet, M. P., Przekop, A., Rizzi, S. A., and Spottswood, S. M., "A review of indirect/non-intrusive reduced order modeling of nonlinear geometric structures," *Journal of Sound and Vibration*, Vol. 332, No. 10, 2013, pp. 2437–2460.

[11]Luelf, F. A., Tran, D.-M., and Ohayon, R., "Reduced bases for nonlinear structural dynamic systems: A comparative study," *Journal of Sound and Vibration*, Vol. 332, No. 15, 2013, pp. 3897–3921.

[12]Placzek, A., Tran, D.-M., and Ohayon, R., "A nonlinear POD-Galerkin reduced-order model for compressible flows taking into account rigid body motions," *Computer Methods in Applied Mechanics and Engineering*, Vol. 200, No. 49, 2011, pp. 3497–3514.

[13]Lucia, D. J., Beran, P. S., and Silva, W. A., "Reduced-order modeling: new approaches for computational physics," *Progress in Aerospace Sciences*, Vol. 40, No. 1, 2004, pp. 51–117.

[14] Dowell, E., Edwards, J., and Strganac, T., "Nonlinear aeroelasticity," *Journal of aircraft*, Vol. 40, No. 5, 2003, pp. 857–874.

[15] Dowell, E. H., *A modern course in aeroelasticity*, Kluwer Academic Publishers, 4th ed., 2004.

[16] Tantaroudas, N., Ronch, A. D., Badcock, K., and Palacios, R., "Model Order Reduction for Control Design of Flexible Free-Flying Aircraft," *56th AIAA Atmospheric Flight Mechanics Conference*, Kissimmee, FL, 2015.

[17] Demasi, L. and Livne, E., "Dynamic aeroelasticity of structurally nonlinear configurations using linear modally reduced aerodynamic generalized forces," *AIAA Journal*, Vol. 47, No. 1, 2009, pp. 70–90.

[18] Hodges, D. H., "Geometrically exact, intrinsic theory for dynamics of curved and twisted anisotropic beams," *AIAA Journal*, Vol. 41, No. 6, 2003, pp. 1131–1137.

[19] Wynn, A., Wang, Y., Palacios, R., and Goulart, P. J., "An energy-preserving description of nonlinear beam vibrations in modal coordinates," *Journal of Sound and Vibration*, Vol. 332, No. 21, 2013, pp. 5543–5558.

[20] Palacios, R., Wang, Y., and Karpel, M., "Intrinsic models for nonlinear flexible-aircraft dynamics using industrial finite-element and loads packages," *53rd AIAA/ASME/ASCE/AHS/ASC Structures, Structural Dynamics and Materials Conference*, Honolulu, Hawaii, USA, April 2012, AIAA Paper No 2012-1401.

[21] Peters, D. A., "Two-dimensional incompressible unsteady airfoil theory–An overview," *Journal of Fluids and Structures*, Vol. 24, No. 3, 2008, pp. 295–312.

[22] Katz, J. and Plotkin, A., *Low-Speed Aerodynamics*, Cambridge University Press, 2001.

[23] Patil, M. J. and Hodges, D. H., "Flight dynamics of highly flexible flying wings," *Journal of Aircraft*, Vol. 43, No. 6, 2006, pp. 1790–1799.

[24] Bauchau, O. A. and Trainelli, L., "The vectorial parameterization of rotation," *Nonlinear dynamics*, Vol. 32, No. 1, 2003, pp. 71–92.

[25] Glover, K. and Doyle, J. C., "State-space formulae for all stabilizing controllers that satisfy an H-norm bound and relations to relations to risk sensitivity," *Systems & Control Letters*, Vol. 11, No. 3, 1988, pp. 167–172.

[26] Goland, M., "The Flutter of a Cantilever Wing," *Journal of Applied Mechanics*, Vol. 12, No. 4, 1945, pp. 197–208.

[27] Sotoudeh, Z., Hodges, D., and Chang, C., "Validation Studies for Aeroelastic Trim and Stability Analysis of Highly Flexible Aircraft," *Journal of Aircraft*, Vol. 47, No. 4, 2010, pp. 1240–1247.

[28] Murua, J., Palacios, R., and Graham, J. M. R., "Assessment of Wake-Tail Interference Effects on the Dynamics of Flexible Aircraft," *AIAA Journal*, Vol. 50, No. 7, 2012, pp. 1575–1585.

[29] Hesse, H. and Palacios, R., "Consistent structural linearisation in flexible-body dynamics with large rigid-body motion," *Computers & Structures*, Vol. 110, 2012, pp. 1–14.

[30] Wang, Y., Palacios, R., and Wynn, A., "A method for normal-mode-based model reduction in nonlinear dynamics of slender structures," *Computers & Structures*, Vol. 159, 2015, pp. 26–40.

[31] Moulin, B., Idan, M., and Karpel, M., "Aeroservoelastic structural and control optimization using robust design schemes," *Journal of Guidance Control and Dynamics*, Vol. 25, No. 1, 2002, pp. 152–159.

[32] Skogestad, S. and Postlethwaite, I., *Multivariable Feedback Control: Analysis and Design*, Vol. 2, Wiley New York, 2007.